

1 **Revision 2**

2

3 **Tourmaline chemical and boron isotopic constraints on the**  
4 **magmatic-hydrothermal transition and rare-metal mineralization in alkali**  
5 **granitic systems**

6

7 HUAN-HUAN WU<sup>1,2,3,4</sup>, HE HUANG<sup>1\*</sup>, ZHAO-CHONG ZHANG<sup>2</sup>, SHUI-YUAN YANG<sup>5</sup>,

8

YONG-BAO GAO<sup>3</sup>, ADRIAN A. FINCH<sup>4</sup>

9 <sup>1</sup> SinoProbe Laboratory, Institute of Geology, Chinese Academy of Geological Sciences, Beijing 100037,

10

P.R. China

11 <sup>2</sup>State Key Laboratory of Geological Processes and Mineral Resources, China University of Geosciences,

12

Beijing 100083, P.R. China

13 <sup>3</sup>Xi'an Center of Mineral Resources Survey, China Geological Survey, Xi'an 710100, P.R. China

14

<sup>4</sup>School of Earth & Environmental Sciences, University of St Andrews, KY16 9TS, UK

15 <sup>5</sup>State Key Laboratory of Geological Processes and Mineral Resources, China University of Geosciences,

16

Wuhan 430074, P.R. China

17

18

## ABSTRACT

19       The magmatic-hydrothermal transition in granite-related rare-metal metallogenic  
20 systems has received great attention, as economic rare metal (including rare earth)  
21 minerals reach saturation and trigger mineralization at this stage. However, deciphering  
22 the details of the melt-fluid evolution process and the distribution behavior of rare  
23 metals remains difficult. Here, we applied tourmaline chemistry and B isotopes to  
24 unravel processes at the magmatic-hydrothermal transition that are responsible for  
25 rare-metal partitioning in the Huoshibulake (HS) and Tamu (TM) REE-Nb-mineralized  
26 intrusions in Southern Tianshan, SW Central Asian Orogenic Belt. Three types of  
27 tourmaline are identified in the plutons: (1) disseminated tourmaline in the granite, with  
28 a brown-yellow core (HS-DB) and blue-green rim (HS-DG); (2) orbicular tourmaline,  
29 with a brown-yellow core (HS-OB and TM-OB) and blue-green rim (HS-OG and  
30 TM-OG); (3) vein tourmaline (HS-V and TM-V). Compositionally, all these  
31 tourmalines exhibit extremely low Ca and Mg contents and are classified as schorl. The  
32 substitution processes of major-element variations are dominantly caused by (Al, □)  
33 (Fe, Na)<sub>-1</sub> exchange vectors. Four generations of tourmaline crystallization are  
34 established based on the petrographic, compositional, and B isotopes evolution of the  
35 tourmaline. Firstly, the HS-DB crystals crystallized from the highly evolved residual  
36 melt, and then HS-OB and TM-OB precipitated from immiscible B-rich aqueous melts  
37 during the magmatic-hydrothermal transition. Subsequently, the blue-green  
38 overgrowths (HS-DG, HS-OG, and TM-OG) crystallized from exsolved hydrothermal  
39 fluids. Finally, the formation of HS-V and TM-V resulted from another melt pulse from

40 a deeper magma chamber. The magmatic tourmaline exhibits a narrow range of  $\delta^{11}\text{B}$   
41 values between -12.6 to -10.0‰, while the hydrothermal tourmaline shows  
42 significantly heavier and variable  $\delta^{11}\text{B}$  values ranging from -10.2 to -4.9‰. The  
43 fractionation of B isotopes is reproduced by Rayleigh fractionation modeling. Lower  
44 Nb and Sn contents in the orbicular tourmaline relative to those precipitated from the  
45 residual melt, along with the lack of rare-metal minerals in the orbicules, indicate that  
46 B-rich melt/fluid exsolution does not necessarily contribute to the rare-metal  
47 mineralization. In comparison, the veins contain abundant rare-metal and REE minerals  
48 in close paragenesis with fluorite, and the vein tourmaline shows high Nb and Sn  
49 contents. These observations suggest that saturation of fluorite triggered the  
50 precipitation of rare metals, and fluorine played a critical role in rare metal  
51 concentration and mineralization. This study highlights the potential of tourmaline to  
52 trace the magmatic-hydrothermal transition and provide insights into rare-metal  
53 mineralization in the granitic systems.

54 **Keywords:** Multi-generation tourmaline, boron isotopes, magmatic-hydrothermal  
55 transition, rare-metal mineralization

56

57

## INTRODUCTION

58 The magmatic-hydrothermal transition, during which the  
59 crystallization/fractionation of orthomagmatic systems evolves from melt-driven  
60 (magmatic) to fluid-driven (hydrothermal) processes, is still poorly understood  
61 because of the transient timescale and widespread overprints by post-magmatic,  
62 low-temperature alteration ([Halter and Webster, 2004](#); [Michaud and Pichavant, 2020](#)).  
63 During the transition, complex melt-fluid interactions involving silicic melts, aqueous  
64 melts, and hydrothermal fluids occur ([Kaeter et al., 2018](#); [Thomas et al., 2012](#)).  
65 Although it has been acknowledged that rare-metal granites generally originate from  
66 a fertile source with low-degree partial melting and high-degree fractional  
67 crystallization contributing significantly to rare-metal enrichment ([Ballouard et al.,](#)  
68 [2020](#); [Linnen et al., 2014](#); [Sheard et al., 2012](#); [Williams-Jones and Vasyukova, 2023](#)),  
69 evidence increasingly points towards the magmatic-hydrothermal transition as the  
70 critical stage to achieve the hyper-enrichment and mineralization of rare metals  
71 ([Ballouard et al., 2016](#); [Carr et al., 2021](#); [Zhu et al., 2015](#)). However, clarifying the  
72 distribution behavior of rare-metal elements and their metallogenic mechanism  
73 during the transition remains challenging.

74 Tourmaline is a common borosilicate mineral in granitic systems that can  
75 crystallize directly from the early magmatic stage through to the late sub-solidus fluid  
76 ([Liu and Jiang, 2021](#); [Yang et al., 2015](#)). Due to its highly variable composition,  
77 stability over large P-T ranges, and resistance to post-crystallization alteration,  
78 tourmaline has been regarded as a reliable monitor for tracing the evolution of

79 melts/fluids composition ([Dutrow and Henry, 2011](#); [Hong et al., 2019](#); [Jiang et al.,](#)  
80 [2004](#); [Slack and Trumbull, 2011](#); [van Hinsberg et al., 2011](#)). In particular, the  
81 differential distribution behavior of  $^{11}\text{B}$  and  $^{10}\text{B}$  between melts and fluids makes boron  
82 isotopes in tourmaline a potentially valuable indicator for deciphering  
83 magmatic-hydrothermal processes ([Drivenes et al., 2015](#); [Qiu et al., 2021](#); [Zhao et al.,](#)  
84 [2021a](#)).

85 The Atushi-Baicheng-Yuli alkaline rock belt, located in South Tianshan, is a  
86 transitional zone between the Central Asian Orogenic Belt and Tarim Craton and it is  
87 composed of outcrops of alkali granite, syenite, and carbonatite, some of which host  
88 world-class rare-metal (Nb-REE) deposits (e.g., Boziguo'er Nb-REE deposit, [Huang](#)  
89 [et al., 2018](#); the Wajilitag REE deposit, [Cheng et al., 2018](#); the Kuoketag Nb-REE  
90 deposit, [Chen et al., 2002](#)). The Huoshibulake (HS) and Tamu (TM) plutons are  
91 adjacent A-type granitic plutons in the Atushi district with Nb and REE  
92 mineralization, characterized by a wide occurrence of economic minerals, e.g., most  
93 importantly columbite, synchysite, fluocerite ([Shi et al., 2010](#)). Tourmaline occurs in  
94 many forms in the plutons, including disseminated, orbicular, and veins, the latter two  
95 intimately with quartz. It records a continuous evolution from the magmatic to  
96 hydrothermal stages. Tourmaline-quartz orbicules occur widely in the two alkali  
97 granitic plutons, a texture most commonly reported in peraluminous granitic systems  
98 and considered a product of segregated B-rich melts ([Drivenes et al., 2015](#); [Harlaux et](#)  
99 [al., 2020](#); [Hong et al., 2019](#); [Zhao et al., 2021a](#)). These plutons show varying degrees  
100 of rare-metal mineralization in the different stages, and rare-metal minerals exhibit

101 paragenesis with specific generations of tourmaline. Consequently, the two alkali  
102 plutons offer an exceptional natural laboratory for elucidating the  
103 magmatic-hydrothermal transition and associated rare-metal mineralization within the  
104 alkali granitic systems, from the perspective of tourmaline.

105 In this study, we carry out detailed investigations on tourmaline from the two  
106 plutons, including mineral textures, chemical compositions, and B isotopes, to  
107 reconstruct the magmatic-hydrothermal evolution. We further constrain the  
108 distribution and precipitation of Nb and REE during the magmatic-hydrothermal  
109 transition by integrating the paragenesis of economic minerals with the different types  
110 of tourmaline as well as by evaluating variations of the ore-forming elements in the  
111 tourmaline.

## 112 **GEOLOGICAL BACKGROUND**

113 The Central Asian Orogenic Belt (CAOB) is one of the largest accretionary orogens  
114 in the world, sandwiched between the Siberian and European Cratons to the north and  
115 the Karakum-Tarim-North China Cratons to the south. The Western Xinjiang region is  
116 situated in the southwestern CAOB and can be divided into (from north to south) the  
117 Altay, Junggar Block, North Tianshan Belt (NTB), Yili-Kazakhstan Block (YKB),  
118 Central Tianshan Block (CTB), South Tianshan Belt (STB), and northern margin of the  
119 Tarim Craton (NMTC) ([Figure 1a](#)). The STB is bounded by the Southern-Central  
120 Tianshan Suture (SCTS) to the north and by the North Tarim Suture (NTS) to the south  
121 and resulted from the Paleozoic closure of the Paleo-Asian Ocean and the subsequent  
122 collision of Tarim Block and Southwestern CAOB. During the Early Permian, the

123 northern margin of Tarim and its adjacent areas was subjected to intracontinental  
124 extension, accompanied by regional alkaline magmatism (Wei et al., 2019; Zong et al.,  
125 2020). From Atushi in the west to Yuli in the east, this created a series of alkaline  
126 volcanic and intrusive rocks, forming a ~1100 km long alkaline-rock belt. Several rare  
127 metal deposits (e.g., Boziguo'er Nb-Ta-Zr deposit, Kuoketag Nb-Ta-Zr deposit, and  
128 Wajilitag REE deposit) and rare metal mineralized plutons (e.g., Tamu  
129 Nb-REE-mineralized pluton, Huoshibulake REE-mineralized pluton, and  
130 Bashisuogong Nb-REE complex) have been found in the belt (Nechaev et al., 2021; Xie  
131 et al., 2021), revealing significant rare-metal metallogenic potential in the area.

132 The Huoshibulake and Tamu plutons are situated in the north-east of Atushi city  
133 (Figure 1a). The Huoshibulake pluton has an outcrop of 30 km<sup>2</sup> and consists of two  
134 transitional units from the center outward: biotite granite and biotite K-feldspar granite  
135 (Figures 1b and 2a). The Tamu pluton, located ~10 km southwest of the Huoshibulake  
136 pluton (Figure 1c), shows similar petrographic features to the Huoshibulake pluton.  
137 The major minerals in both plutons are alkali feldspar, quartz, biotite, and minor alkali  
138 amphibole, fluorite, and tourmaline. Major economic rare metal (including REE)  
139 minerals consist of monazite, columbite, synchysite, and fluocerite. Both plutons  
140 exhibit high SiO<sub>2</sub> (74.6–78.1 wt%), Al<sub>2</sub>O<sub>3</sub> (11.5–12.6 wt%), and total alkali (7.85–8.96  
141 wt%) contents, while having extremely low CaO (0.10–1.22 wt%) and MgO (0.02–  
142 0.22 wt%) contents (Huang et al., 2012). Multi-mineral U-Pb dating of both plutons  
143 yielded an identical age of ~273 Ma, revealing the early Permian emplacement (Wu et  
144 al., in preparation).

## 145                   **TOURMALINE OCCURRENCE AND SAMPLE DESCRIPTIONS**

146           Tourmaline is widespread and shows similar features in both the Huoshibulake and  
147 Tamu plutons. Based on the textural characteristics, three distinct types of tourmaline  
148 are identified: (1) disseminated subhedral to anhedral tourmaline in granite matrix; (2)  
149 tourmaline in tourmaline-quartz orbicules (termed “orbicular tourmaline” in this paper);  
150 and (3) tourmaline in tourmaline-quartz veins. The characteristics of these tourmalines  
151 are described as follows:

### 152   **Disseminated tourmaline in the Huoshibulake pluton**

153           Disseminated tourmaline is found in most granite samples from the Huoshibulake  
154 pluton (Figure 2b, c) but is absent in the Tamu pluton. Tourmaline grains of this type  
155 are distributed within the granitic matrix as isolated subhedral to anhedral grains  
156 (Figure 2d, e) or grain aggregates (Figure 2f), tens to hundreds of micrometers long,  
157 commonly coexisting with quartz, biotite, and K-feldspar grains. They generally  
158 contain yellow-brown (abbreviated as HS-DB, where ‘HS’, ‘D’, and ‘B’ represent  
159 pluton name, texture, and color of tourmaline; similar rules apply to the abbreviations  
160 used below) mantles with occasional blue-green rims (HS-DG), which are also  
161 distinguished from each other by different degrees of back-scattered brightness in the  
162 back-scattered electron images (BSE, Figure 2g–i). A notable phenomenon is a large  
163 abundance of rare-metal minerals (e.g., zircon, monazite, columbite, synchysite,  
164 fluorite) enclosed in these disseminated tourmalines (Figures 2g–i and 3a–c). These  
165 rare-metal minerals are highly concentrated in close proximity to fluorite (Figure 3a–c).

## 166 **Tourmaline in tourmaline-quartz orbicules**

167 Tourmaline–quartz orbicules have a widespread occurrence in both Huoshibulake  
168 and Tamu plutons (Figure 1b, c). The orbicules are randomly distributed and  
169 commonly several to more than ten centimeters in diameter (Figure 4a, b). A typical  
170 orbicule consists of a tourmaline core, a tourmaline-quartz mantle, and a leucocratic  
171 rim (Figure 4b). The core consists mainly of clusters of euhedral tourmaline with minor  
172 quartz grains, whereas tourmaline (~50 vol.%) is intergrown with quartz (~40 vol.%) in  
173 the mantle, along with minor relicts of partially-replaced perthitic K-feldspar (~10  
174 vol.%). Minor biotite, muscovite, and fluorite are also present in the orbicules, but  
175 rare-metal minerals are lacking. A 0.5–1 cm wide leucocratic rim can be recognized  
176 surrounding the orbicules. The fine-grained granitic-textured rim is compositionally the  
177 same as the surrounding granite, but with lower proportions of mafic minerals. The  
178 tourmaline in orbicules shows a sieve-like texture characterized by the intergrowth of  
179 tourmaline and quartz (Figure 4c, d). Two types of tourmaline are distinguishable in  
180 plane-polarized light: tourmaline at the core of the crystals shows yellow to brown  
181 pleochroism (HS-OB and TM-OB), and tourmaline at the rim exhibits green to blue  
182 pleochroism (HS-OG and TM-OB) (Figure 4c, d). When viewed using BSE imaging,  
183 the green rims consistently show lower brightness than the brown cores (Figure 4e, f).

## 184 **Tourmaline in tourmaline-quartz vein**

185 Tourmaline-quartz veins are well developed in the Huoshibulake and Tamu  
186 plutons, with variable widths ranging from several to tens of centimeters and lengths  
187 from several to tens of meters (Figure 5a, b). Most veins exhibit near-vertical

188 orientation and are generally parallel in the same outcrop (Figure 5a). These veins are  
189 composed mainly of tourmaline and quartz, with minor muscovite and fluorite (Figure  
190 5c). The tourmaline from these veins (HS-V and TM-V) exhibits yellow to blue  
191 pleochroism; most grains show distinct growth zonation (Figure 5d–f), which is also  
192 recognizable in the BSE images (Figure 5g–i). A large number of rare-earth minerals  
193 (e.g., synchysite, fluocerite, and monazite) and columbite are observed in these veins  
194 (Figure 3d–f) in contrast to the orbicules. Most rare-metal minerals are precipitated as  
195 inclusions in, or near, fluorite (Figure 3e, f).

## 196 ANALYTICAL METHODS

### 197 Electron probe microanalysis (EPMA)

198 The major and minor elements of tourmaline were analyzed with a JEOL  
199 JXA-8230 Electron Probe Microanalyzer equipped with five wavelength-dispersive  
200 spectrometers (WDS) at the Laboratory of Microscopy and Microanalysis, Wuhan  
201 Microbeam Analysis Technology Co., Ltd. The samples were coated with a thin  
202 conductive carbon film before analysis. The precautions suggested by Zhang and Yang  
203 (2016) were used to minimize the difference in carbon film thickness between samples  
204 and obtain a ca. 20 nm approximately uniform coating. Operating conditions for  
205 quantitative WDS analyses involved an accelerating voltage of 15 kV, a beam current  
206 of 20 nA, and a 10  $\mu\text{m}$  spot size. Data were corrected online using a ZAF (atomic  
207 number, absorption, fluorescence) correction procedure. The content of B was  
208 calculated based on the mole ratio of B:Si = 1:2, and then involved in the ZAF  
209 correction procedure. The peak counting time was 10 s for Ca, Mg, K, F, Si, Al, Ti, Na,  
210 and Cl, and 20 s for Fe and Mn. The background counting time was 1/2 of the peak  
211 counting time on the high- and low-energy background positions. The following

212 standards were used: diopside (Ca, Mg), microcline (K), barium fluoride (F), olivine  
213 (Si), pyrope garnet (Fe, Al), jadeite (Na), halite (Cl), rutile (Ti), rhodonite (Mn).

#### 214 **LA-ICP-MS and LA-MC-ICP-MS analysis**

215 In situ trace-element analyses of tourmaline were conducted at the State Key  
216 Laboratory of Geological Processes and Mineral Resources (GPMR) in China  
217 University of Geosciences (Wuhan), using a RESolution S-155 laser ablation system  
218 coupled to a Thermo iCAP-Q<sub>c</sub> inductively coupled plasma-mass spectrometer  
219 (LA-ICP-MS). The U.S. Geological Survey (USGS) reference glasses (BIR-1G,  
220 BCR-2G, and BHVO-2G) and the NIST SRM 612 and 610 glasses were analyzed after  
221 every eight tourmaline sample spots. The ablation protocol employed a spot diameter of  
222 33 μm at a 10 Hz repetition rate for 40 s. The approximate depth of ablation was 30–50  
223 μm. Helium was used as the carrier gas to the ICP-MS. The isotope <sup>29</sup>Si was used as the  
224 internal standard in conjunction with the Si concentrations determined by EPMA.  
225 External calibration was performed using the USGS reference glasses. The NIST  
226 glasses were used for correcting the signal drift. Raw data reduction was performed  
227 offline using the ICPMSDataCal software (Liu et al., 2010), and to reduce the effect of  
228 the signal variability with depth on the test results, the same integration interval of the  
229 signal was chosen for the sample and standard.

230 Most of the in situ B isotopic compositions of tourmaline were measured at the  
231 GPMR using the same laser ablation system coupled to a Nu Plasma II multicollector  
232 ICP-MS. Additional analyses were conducted at the National Research Center for  
233 Geoanalysis, Chinese Academy of Geological Science (CAGS), using a Neptune Plus

234 fs-LA-MC-ICP-MS (Thermon Fisher Scientific, Germany) in combination with a 343  
235 nm femtosecond laser ablation system (J-100, Applied Spectra, West Sacramento, CA,  
236 USA). Both analyses were carried out with a beam diameter of 50  $\mu\text{m}$  and a 10 Hz  
237 repetition rate. The  $^{11}\text{B}$  and  $^{10}\text{B}$  were collected statically and simultaneously with two  
238 Faraday cups. The instrumental mass fractionation (IMF) was calibrated using the  
239 sample standard bracketing (SSB) method. The international tourmaline standard IAEA  
240 B4 ( $\delta^{11}\text{B} = -8.71\text{‰}$ ; [Tonarini et al., 2003a](#)) was adopted as the external standard during  
241 the two analyses. The similarity of IMF values ([Online Materials Table OM2](#))  
242 determined for the chemically distinct tourmaline standards, including two in-lab  
243 tourmaline reference materials used at the GPMR (schorl HS#112566 and dravite  
244 HS#108796 from the Harvard Mineralogical Museum, [Dyar et al., 2001](#)) and one used  
245 at the CAGS (IMR RB1, [Hou et al., 2010](#)), all demonstrate insignificant matrix effects.  
246 The analytical precision is estimated to be better than 0.5‰ ( $\pm 2\sigma$ ) based on the  
247 replicated analyses of reference tourmaline during this study. More detailed  
248 descriptions of the two analytical methods can be found in [Zhao et al. \(2021a\)](#) and [Long](#)  
249 [et al. \(2021\)](#), respectively. Ten replicated spots were arranged to monitor the analytical  
250 errors between the two labs, and the results showed near identical  $\delta^{11}\text{B}$  values between  
251 the two analyses (all less than 0.2‰, see details in [Online Materials Table OM2](#)).

## 252 RESULTS

### 253 Major element compositions

254 A total of 264 spots among 37 tourmaline grains were analyzed by EPMA, and the  
255 results are given in [Online Materials Table OM1](#). Structural formulae were calculated

256 based on the general formula of  $XY_3Z_6T_6O_{18}(BO_3)_3V_3W$ , where  $X = Ca^{2+}, Na^+, K^+, X_{vac}$   
257 (vacancy);  $Y = Mg^{2+}, Fe^{2+}, Mn^{2+}, Al^{3+}, Ti^{4+}, Fe^{3+}$ ;  $Z = Mg^{2+}, Al^{3+}, Fe^{3+}$ ;  $T = Si^{4+}, Al^{3+}$ ,  
258 ( $B^{3+}$ );  $V = OH^-, O^{2-}$ ; and  $W = OH^-, F^-, O^{2-}$  (Henry et al., 2011). Tetrahedral and  
259 octahedral sites (T+Z+Y) were normalized to 15 cations apfu (atoms per formula unit).

260 Overall, comparable to those of tourmalines crystallized from peraluminous  
261 granitic systems (e.g., Zhao et al., 2019; Zhao et al., 2022), all tourmaline samples from  
262 the Huoshibulake and Tamu plutons show relatively high  $SiO_2$  (32.50–36.03 wt%),  
263  $Al_2O_3$  (21.77–33.21 wt%),  $FeO^T$  (13.98–24.64 wt%) contents, and low  $TiO_2$  (0.00–2.95  
264 wt%),  $MnO$  (0.00–0.15 wt%),  $MgO$  (0.00–1.19 wt%),  $CaO$  (0.00–1.69 wt%),  $Na_2O$   
265 (1.69–2.57 wt%),  $K_2O$  (0.008–0.18 wt%),  $F$  (0.00–1.24 wt%), and  $Cl$  (<0.07 wt%)  
266 contents. Notably, most tourmaline shows extremely low  $CaO$  contents (mostly < 0.1  
267 wt%), except for the HS-DB ones that exhibit much higher contents (0.003–1.69 wt%).  
268 According to the X-site occupancy-based classification by Henry et al. (2011), all  
269 tourmalines are members of the alkali series (Figure 6a). In the Al-Fe-Mg ternary  
270 diagrams of Henry and Guidotti (1985), the tourmaline samples studied exhibit a  
271 narrow variation and plots in the field of Li-poor granite (Figure 6b). Moreover, all  
272 tourmaline is Fe-rich and Mg-poor with restricted  $Mg/(Mg+Fe)$  (0.00 to 0.09) and  
273  $Na/(Na+Ca)$  (0.64 to 1.00) ratios, plotting in the field of schorl series on the  $X$   
274  $[\square/(\square+Na)]$  vs.  $Mg/(Mg+Fe)$  and  $X$   $[Na/(Na+Ca)]$  vs.  $Mg/(Mg+Fe)$  diagrams (Figure  
275 7a, b). The blue-green tourmaline (i.e., HS-DG, HS-OG, and TM-OG types) at the rim  
276 exhibits significantly lower Fe and Ti contents but higher Al and X-site vacancy  
277 contents compared to the yellowish-brown tourmaline (HS-DB, HS-OB, and TM-OB

278 types) in the core ([Figure 8a–d](#)). The yellowish-brown tourmaline has higher Ti  
279 contents than those in blue-green ones, consistent with the suggestion by [Trumbull et al.](#)  
280 ([2007](#)) that Ti content in tourmaline is the primary control for pleochroism. Most  
281 tourmaline crystals from HS-DB, HS-OB, HS-V, TM-OB, and TM-V types have >3  
282 apfu Fe and < 6 apfu total Al, while ones from HS-DG, HS-OG, and TM-OG mainly  
283 possess < 3 apfu Fe and > 6 apfu total Al ([Figures 7d and 8a, b](#)).

#### 284 **Trace-element compositions**

285 The trace elements of 187 spots among 29 tourmaline grains were analyzed by  
286 LA-ICP-MS, all of which followed EPMA to ensure spot locations. The results are  
287 listed in [Online Materials Table OM1](#). The median concentrations of most trace  
288 elements range from 0.1 to 10 ppm, while Li, Zn, Ga, and Sn have the highest median  
289 concentrations up to hundreds of ppm, and Sc, Sr, and Ce show median contents of tens  
290 of ppm. Concentrations of some trace elements show large variations over several  
291 orders of magnitude, such as Li (12.8–256 ppm), Zn (70.3–592 ppm), Sr (0.29–602  
292 ppm), Nb (0.12–71.7 ppm), Sn (4.66–2542 ppm), and REE (0.25–170 ppm). In the  
293 Huoshibulake pluton, the earlier tourmaline (HS-DB and HS-OB) exhibits higher Sc,  
294 Ga, Sr, Sn, and Nb and lower Li concentrations than the later tourmaline (HS-DG and  
295 HS-OG, [Figure 8e–j](#)). However, the latest-stage tourmaline in veins (HS-V) shows an  
296 inverse trend and high Sc, Ga, Sr, Sn, and Nb abundances. Similar variations are also  
297 observed in tourmaline from the Tamu pluton (i.e., TM-OG has higher Li and lower Sc,  
298 Ga, Sr, Sn, and Nb contents than those of TM-OB and TM-V). All tourmaline spots  
299 display large total REE abundance variations ([Figure 8k](#)). Besides, variation diagrams

300 of representative element pairs show significant positive correlations between Hf vs. Zr,  
301 Ta vs. Nb, Sr vs. Sn, and Ce vs. La (Figure 9).

### 302 **Boron isotopic composition**

303 A total of 228 B isotopic compositions (including 10 replicated spots for checking  
304 consistency) among 29 tourmaline grains were determined by LA-ICP-MS, and the  
305 results are listed in Online Materials Table OM2 and plotted in Figure 10. The  $\delta^{11}\text{B}$  of  
306 five types of tourmaline from the Huoshibulake pluton range from -12.6 to -5.2‰,  
307 falling in the range of typical granitic magmas (-20 to -5‰, Trumbull and Slack, 2018).  
308 Tourmaline spots from the HS-OB, HS-DB, and HS-V types exhibit restricted ranges of  
309  $\delta^{11}\text{B}$  from -11.8 to -10.2‰ (mean = -10.9‰, n = 26), -12.6 to -10.0‰ (mean = -11.1‰,  
310 n = 30), and -11.7 to -10.1 ‰ (mean = -10.9‰, n = 23), respectively. In comparison,  
311 blue-green tourmaline from HS-OG and HS-DG groups shows significantly higher  
312 values of  $\delta^{11}\text{B}$  ranging from -9.8 to -7.4‰ (mean = -8.7‰, n = 32) and -10.2 to -5.2‰  
313 (mean = -8.2‰, n = 29). The  $\delta^{11}\text{B}$  values of three types of tourmaline from the Tamu  
314 pluton range from -12.6 to -4.9‰. Similar to the isotopic fractionation observed in the  
315 Huoshibulake pluton, tourmaline grains of TM-OB and TM-V types show relatively  
316 lower  $\delta^{11}\text{B}$  values ranging from -12.6 to -10.0‰ (mean = -11.2‰, n = 34) and -12.2 to  
317 -10.3‰ (mean = -11.3‰, n = 26), while the blue-green tourmaline grains from TM-OG  
318 type have higher values ranging from -9.7 to -4.9‰ (mean = -6.8‰, n = 28).

## 319 **DISCUSSION**

### 320 **Formation of tourmaline**

321 The Huoshibulake and Tamu plutons are two adjacent A-type rare-metal granites in

322 the South Tianshan alkaline rock belt. Multi-mineral geochronological studies have  
323 shown both emplaced at ~273 Ma (Zhang et al., 2010; Wu et al., in preparation). They  
324 are both characterized by high SiO<sub>2</sub>, Al<sub>2</sub>O<sub>3</sub>, and alkali contents, low FeO<sup>T</sup>, MgO, and  
325 CaO contents, and enrichment of large ion lithophile elements (e.g., Rb) and high  
326 field-strength elements (e.g., Nb, Ta, Zr, Hf) (Zhang and Zou, 2013; Zong et al., 2020).  
327 Besides, their similar whole-rock Nd isotopes and zircon Hf-O isotopes are consistent  
328 with them being genetically related (Wei et al., 2019; Zhang and Zou, 2013). Combined  
329 with their indistinguishable petrographic features, Huang et al. (2012) concluded that  
330 they are twin plutons derived from a single deeper magma chamber in a multi-level  
331 plumbing system, which ultimately originated from low-pressure partial melting of the  
332 mafic lower crust.

333 A distinct characteristic of the Huoshibulake and Tamu plutons is the widespread,  
334 multi-generation crystallization of tourmaline. Consistent with the whole-rock  
335 composition, all types of tourmaline in the two plutons show extremely low CaO (0–  
336 1.68 wt%) and MgO (0–1.19 wt%) contents, indicating their crystallization from  
337 highly evolved magmatic-hydrothermal systems (Zheng et al., 2022). In the Mg-Fe  
338 plot, tourmalines from the two plutons do not show any observable substitution trend of  
339 MgFe<sub>-1</sub> function because of low Mg contents but reveal a substitution trend consistent  
340 with the FeAl<sub>-1</sub> function (Figure 7c). The higher Fe and total Al contents in tourmaline  
341 crystals from the yellowish-brown tourmaline (HS-DB, HS-OB, and TM-OB types)  
342 than those of blue-green tourmaline (HS-DG, HS-OG, and TM-OG types) suggests that  
343 Fe could be incorporated into the Z-site to substitute Al (up to 1.11 apfu in this study)

344 when Al is deficient. Conversely, Al can be incorporated into the Y-site to substitute Fe  
345 (up to 0.77 apfu in this study) when Al became elevated to excess in the Z-site during  
346 magmatic evolution. The charge balance is maintained by the adjustment of vacant  
347 X-site or substitution between O and OH (Figure 7e). The HS-DB tourmaline in the  
348 Huoshibulake pluton is disseminated interstitially between quartz and K-feldspar,  
349 brown in color without fine-scale zonation (Figure 2d–f), and in some cases, the rim  
350 of HS-DB tourmaline is replaced by K-feldspar with a few small irregular tourmaline  
351 residues (Figure 2e), consistent with the characteristics of magmatic tourmaline in  
352 other highly evolved granites (Zhao et al., 2021a; Zhao et al., 2019; Yang et al., 2015).  
353 The Mg/(Mg+Fe) ratio generally decreases with magmatic differentiation (Yang et al.,  
354 2015); higher Mg/(Mg+Fe) ratios of the HS-DB tourmaline compared to other  
355 tourmaline types (Figure 7a, b) are consistent with earlier crystallization of the  
356 HS-DB tourmaline. This is also supported by the linear relationships shown in the  
357 plots of  $Al^{tot}$  vs.  $Fe^{tot}$  and  $Al^{tot}$  vs. X-site vacancy that the compositional evolution of  
358 most tourmaline types in the Huoshibulake and Tamu plutons were mainly controlled  
359 by exchange of  $(Al, \square) (Fe, Na)_{-1}$  while the HS-DB show an exchange trend of  $(Al, Na)$   
360  $(Ca, Mg)_{-1}$  (Figure 7d–f). Thus, we conclude that the HS-DB tourmaline is of primary  
361 magmatic origin.

362 Tourmaline-quartz orbicules have been widely reported in evolved peraluminous  
363 granitic rocks with different tectonic settings and ages worldwide (Yang et al., 2015;  
364 Trumbull et al., 2007). However, they have rarely been reported in alkali granitic  
365 systems. Although a hydrothermal origin related to post-magmatic alteration has been

366 proposed in some studies (e.g., [Rozendaal and Bruwer, 1995](#)), the orbicules are more  
367 commonly interpreted as crystallization products of late-magmatic, volatile-rich melts  
368 in which volatile-rich phases are incapable of escaping from the magmatic system  
369 ([Balén and Broska, 2011](#); [Trumbull et al., 2007](#); [Yang et al., 2015](#)). The  
370 tourmaline-quartz orbicules in the Huoshibulake and Tamu plutons are isolated in the  
371 granites without fracture networks or veinlets (denoting fluid pathways) connecting  
372 them to the surrounding rock ([Figure 4a, b](#)). Besides, the orbicular tourmaline exhibits  
373 extremely low Mg and Ca contents, inconsistent with the origination of external fluids  
374 that are generally rich in Mg and Ca ([Slack, 1996](#); [Trumbull et al., 2007](#)). Some  
375 trace-element pairs (e.g., Nb-Ta, [Ballouard, et al., 2016](#); Zr-Hf, [Zaraisky, et al., 2009](#))  
376 show similar enrichment behaviors during magmatic-hydrothermal evolution. The  
377 positive correlations of these element pairs shown in [Figure 9](#) are consistent with a  
378 continuous magmatic-hydrothermal evolution trend. It has been proposed that an  
379 aqueous melt phase, rich in fluxing elements (e.g., P, Li, B, and F), can separate from  
380 the residual melt at the final stage of highly evolved granitic systems ([Balén and](#)  
381 [Broska, 2011](#); [Thomas et al., 2005](#); [Veksler et al., 2002](#)). Evidence from both  
382 experiments and melt inclusions in natural samples reveals that B has a higher affinity  
383 for partitioning into such an aqueous melt compared with normal aluminosilicate melt  
384 and aqueous fluid ([Thomas et al., 2003](#); [Veksler et al., 2002](#)). In our case, the similar  
385 pleochroism and B isotopic compositions of the HS-OB and HS-DB tourmalines  
386 allow their crystallization from compositionally and isotopically similar melts. For  
387 these reasons, the tourmaline orbicules are interpreted to form from immiscible B-rich

388 aqueous melts during the magmatic-hydrothermal transition. The lower Mg/(Mg+Fe)  
389 ratios of the HS-OB tourmaline relative to the HS-DB ones can be attributed to the  
390 precipitation of biotite before the exsolution of the immiscible B-rich melts,  
391 analogous to the scenario of Qitianling granite in South China (Yang et al., 2015).  
392 Feldspar is the major Sr-bearing mineral in the Huoshibulake pluton; the lower Sr  
393 contents of the HS-OB (2.82–44.8 ppm) tourmaline compared to HS-DB ones (11.9–  
394 602 ppm) are consistent with the later formation of tourmaline-quartz orbicules.  
395 Overgrowths of green-blue tourmaline (HS-DG, HS-OG, and TM-OG types) around  
396 brown cores (HS-DB, HS-OB, and TM-OB types) show sharp changes in both  
397 elemental and B isotopic compositions, precluding progressive crystallization and  
398 revealing a change of the crystallization medium. Analogous characteristics have also  
399 been reported in highly evolved peraluminous granites and interpreted as the  
400 transition of tourmaline formation from a silicate melt-dominated to hydrothermal  
401 environments (e.g., Zhao et al., 2022, Drivenes et al., 2015, Trumbull et al., 2020).  
402 Compared with the brown tourmaline, the green-blue overgrowths exhibit lower Ca,  
403 Na, Ti, and Fe contents and higher X-site vacancy (Figure 8a–d). The significantly  
404 higher Sr and Sc and lower Li contents of the brown tourmaline than those of  
405 green-blue tourmaline (Figure 8e–g) agree with the partition preference that Sr and Sc  
406 strongly partition in melt while Li is highly fluid mobile (Bai and Van Groos, 1999;  
407 Penniston-Dorland et al., 2012). Besides, the stronger B isotopic fractionation during  
408 crystallization of tourmaline from fluids than that from melts generally causes  
409 significantly heavier B isotopic compositions in hydrothermal tourmaline than in

410 magmatic tourmaline (see details in the next section), consistent with the fractionation  
411 observed in this study (Figure 10). In combination with its occurrence in both  
412 disseminated and orbicular tourmaline groups, the green-blue tourmaline is  
413 interpreted as a hydrothermal origin and precipitated from later exsolved fluids in the  
414 magmatic-hydrothermal transition.

415 Both external fluid activity and exsolved magmatic-hydrothermal melt/fluid at the  
416 latest stage of magmatic evolution could account for tourmaline-quartz veins (Zhao et  
417 al., 2019). However, the extremely low Ca and Mg contents of the vein tourmaline  
418 argue against an external origin involving the country rocks which mainly consist of  
419 calcareous sandstone and limestone (Shuai et al., 2019). The tourmaline-quartz veins  
420 in the Huoshibulake and Tamu plutons show straight and sharp boundaries with the  
421 host granite (Figure 5a, b). Most of these veins have near-vertical orientation and are  
422 generally parallel in the same outcrop (Figure 5a), indicating that they intruded along  
423 fractures after the granites solidified. U-Pb dating of the cassiterite from the  
424 tourmaline-quartz vein yields a coeval age ( $271\pm 4$  Ma) with the host granite ( $275\pm 2$   
425 Ma), suggesting that they formed within the same magmatic event (Wu et al., in  
426 preparation). Besides, the indistinguishable elemental (Figures 8 and 9) and B isotopic  
427 compositions (Figure 10) of the vein tourmaline with the disseminated tourmaline  
428 permit a similar origin. Based on these lines of evidence, we propose that the  
429 tourmaline-quartz veins were probably the product of highly evolved, B-rich melts of  
430 another magma pulse from a deeper cogenetic magma chamber which emplaced after  
431 the plutons had consolidated.

## 432 **Boron source and variations of boron isotopes**

433 The fractionation of B isotopes in the magmatic-hydrothermal systems is  
434 commonly explained by differential B coordination in different phases since  $^{11}\text{B}$   
435 exhibits a greater tendency to trigonal coordination while  $^{10}\text{B}$  adopts tetrahedral  
436 coordination (Kakihana et al., 1977; Palmer and Swihart, 1996). Boron is  
437 predominately trigonally coordinated in tourmaline and aqueous fluid (Bassett, 1976;  
438 Schmidt et al., 2005); by contrast, B coordination in silicate melt is a mix of both  
439 trigonal and tetrahedral coordination depending on water content, alkali/aluminum  
440 ratio, and speciation of aluminum (Dingwell et al., 1996). Thus,  
441 magmatic-hydrothermal processes involving phase separation (e.g., Rayleigh  
442 fractionation during the crystallization of tourmaline from melts or fluids and isotopic  
443 redistribution during melt/fluid exsolution) would be encoded as differential B isotopic  
444 fractionation (Smith and Yardley, 1996).

445 Due to the lack of experimental determination, the B isotopic fractionation  
446 between silicate melt and tourmaline was generally calculated indirectly by  
447 combining fractionation between melt and fluid ( $\Delta^{11}\text{B}_{\text{melt-fluid}}$ ) and fluid and tourmaline  
448 ( $\Delta^{11}\text{B}_{\text{Tur-fluid}}$ ) in the past decades (e.g., Zhao et al., 2021a, Maner and London, 2017).  
449 However, this method has significant uncertainty since (1) the available  $\Delta^{11}\text{B}_{\text{melt-fluid}}$   
450 and  $\Delta^{11}\text{B}_{\text{Tur-fluid}}$  data were determined by different experimental methods (Cheng et al.,  
451 2022) and (2) the predicted B isotopic fractionation between granitic melt and  
452 tourmaline is much more significant when compared with that observed in the natural  
453 magmatic tourmaline (Kowalski and Wunder 2018; Zhao et al., 2022). Recently, Cheng

454 [et al. \(2022\)](#) reported the first set of experimental data of B isotopic fractionation  
455 between granitic melt and tourmaline, which they defined as  $\Delta^{11}\text{B}_{\text{melt-Tur}} = 4.51 \times$   
456  $(1000/T \text{ [K]}) - 3.94$ . Using the Titanium-in-quartz thermobarometer proposed by  
457 [Huang and Audétat \(2012\)](#), crystallization temperatures of the magmatic tourmaline  
458 paragenic with quartz from the Huoshibulake and Tamu plutons are estimated as 624–  
459 825°C and 614–838°C ([Online Supplementary Material](#)). The small B isotopic  
460 fractionation between melt and magmatic tourmaline ( $\Delta^{11}\text{B}_{\text{melt-Tur}} = -0.26$  at 800 °C and  
461  $-1.23$  at 600 °C) based on the empirical equation is consistent with the limited B  
462 isotopic variation observed in the magmatic tourmaline groups in this study (HS-DB,  
463 HS-OB, HS-V, TM-OB, and TM-V; [Figure 10](#)). With increasing B concentration in the  
464 residual melt, immiscible B-rich magmatic globules could separate from coexisting  
465 granitic magma to form quartz-tourmaline orbicules ([Balen and Broska, 2011](#); [Thomas](#)  
466 [et al., 2005](#)). [Gurenko et al. \(2005\)](#) observed negligible fractionation between  
467 coexisting immiscible B-rich melt and silicate melt. This mechanism explains the  
468 similar B isotopic composition of magmatic tourmaline crystallized from silicate melt  
469 (HS-DB, 12.6‰ to -10.0‰) and those from conjugated aqueous B-rich melts (HS-OB,  
470 -11.8 to -10.2‰; TM-OB, -12.6‰ to -10.0‰). Considering the lightest  $\delta^{11}\text{B}$  value of  
471 -12.6‰, the initial  $\delta^{11}\text{B}$  value of the initial melt is set as -12.3‰. The modeling in  
472 [Figure 11a](#) shows that the slight rise of  $\delta^{11}\text{B}$  values in the magmatic tourmaline can be  
473 reproduced by the combination of increasing  $\delta^{11}\text{B}$  values in the residual melt caused by  
474 Rayleigh fractionation of tourmaline crystallization and the enlargement of  $\Delta^{11}\text{B}_{\text{melt-Tur}}$   
475 along with the decreasing temperature.

476 Both fluid exsolution and Rayleigh fractionation during the crystallization of  
477 hydrothermal tourmaline cause increasing  $\delta^{11}\text{B}$  values in later crystallizing  
478 hydrothermal tourmaline. The experimental data reported by [Hervig et al. \(2002\)](#)  
479 suggested significant B isotopic fractionation between hydrous fluids and silicate melt  
480 of rhyolitic composition at high temperatures (up to  $-7.1\%$ , at  $750\text{ }^\circ\text{C}$  and  $500\text{ MPa}$ ).  
481 [Hervig et al. \(2002\)](#) explained the remarkable  $\Delta^{11}\text{B}_{\text{melt-fluid}}$  by the significant difference  
482 of B coordination between melts (dominantly tetrahedral) and fluids (dominantly  
483 trigonal). However, this result and explanation have been long debated since they  
484 contradict the spectroscopic measurements on synthesized and natural silicate glasses  
485 which show a small amount of or negligible tetrahedral B ([Schmidt et al. 2004](#); [Tonarini](#)  
486 [et al., 2003b](#)). Both the experimental studies and the analysis of melt and fluid  
487 inclusions in evolved granites and pegmatites have revealed that the system changes  
488 from a melt-driven stage to a fluid-driven period at a near-solidus temperature of  
489  $500\text{ }^\circ\text{C}$  ([Thomas et al. 2003](#); [Veksler and Thomas 2002](#)). In this study, given the  
490 heaviest  $\delta^{11}\text{B}$  values of  $-10.0\%$  of the magmatic tourmaline and assuming the fluid  
491 exsolution temperature of  $500\text{ }^\circ\text{C}$ , the  $\delta^{11}\text{B}$  value of the latest melt would be  $\sim -8.1\%$ .  
492 For hydrothermal tourmaline, [Meyer et al. \(2008\)](#) proposed that the B isotopic  
493 fractionation between fluid and tourmaline is temperature-dependent and can be  
494 calculated by  $\Delta^{11}\text{B}_{\text{tour-fluid}} = -4.20 \times [1000/T (\text{K})] + 3.52$ . Considering the most negative  
495  $\delta^{11}\text{B}$  value recorded by HS-DG ( $-10.2\%$ ) and assuming the exsolution temperature of  
496  $500^\circ\text{C}$ , the  $\delta^{11}\text{B}$  value of initial hydrothermal fluid in equilibrium with the late  
497 green-blue tourmaline would be about  $-8.3\%$ . The near-identical estimated B isotopic

498 compositions between the residual melt and the initial fluid imply that the B isotopic  
499 fractionation during fluid exsolution in this study is negligible. Alternatively, the  
500 Rayleigh fractionation modeling shown in [Figure 11b](#) demonstrates that the heavy and  
501 highly variable B isotopic composition of the hydrothermal green-blue tourmaline can  
502 be explained by significant Rayleigh fractionation during the depletion of B in the fluid.  
503 The decrease in temperature can amplify the fluid-tourmaline B isotopic fractionation,  
504 and the heaviest composition (-4.9 ‰ from the TM-OG) can be achieved by ~86%  
505 depletion of B in the residual fluid at 400 °C ([Figure 11b](#)).

506 In summary, the B isotopic variations in the magmatic and hydrothermal  
507 tourmaline observed in the Huoshibulake and Tamu plutons can be reproduced by the  
508 Rayleigh fractionation during the magmatic-hydrothermal transition. Based on the  
509 discussion above, an idealized model is proposed and illustrated in [Figure 12](#).

#### 510 **Rare-metal concentration and precipitation during the magmatic-hydrothermal** 511 **transition in granitic systems**

512 The magmatic-hydrothermal transition has been considered one of the most critical  
513 stages in the granite-related metallogenic system, during which rare metals generally  
514 reach their peak concentrations and precipitate as economic minerals ([Kaeter et al.,](#)  
515 [2018; Ballouard et al., 2020](#)). However, whether the rare metal mineralization in the  
516 granitic system occurs at the melt-driven or fluid-driven stage is still widely disputed  
517 ([Ballouard et al., 2016; Sokół et al., 2021; Yang et al., 2020](#)). Some previous studies  
518 highlighted the role of high-degree fractional crystallization and suggested that the  
519 ore-forming elements are highly concentrated and deposited in the residual melts at the

520 end of the magmatic period (Borodulin et al., 2009; Chevychelov et al., 2005). In  
521 contrast, some studies argued that melt-melt immiscibility or fluid exsolution during  
522 the magmatic-hydrothermal transition could be a critical mechanism for the  
523 hyper-enrichment of rare metals (Ballouard et al., 2016; Thomas and Davidson,  
524 2016), especially when the strongly differentiated distribution of fluxing elements is  
525 involved (Mohamed, 2013; Vasyukova and Williams-Jones, 2014). For instance, some  
526 experimental studies suggested that Nb, Ta, and REE can form complexes with ligands  
527 (e.g., F<sup>-</sup>, Cl<sup>-</sup>) through which they can be effectively concentrated in aqueous melts or  
528 hydrothermal fluids (Migdisov and Williams-Jones, 2014; Timofeev et al., 2015;  
529 Zaraisky et al., 2010). However, little direct evidence from the natural systems has been  
530 found to confirm the trace element distribution behavior during the latest melt-fluid  
531 interaction in the granitic systems.

532 The characteristics of B-rich melt/fluid exsolution in this study provide a unique  
533 insight into the rare metal mineralization during the magmatic-hydrothermal transition.  
534 In the Huoshibulake pluton, HS-DB tourmaline (interpreted as early magmatic)  
535 exhibits high Nb (2.25–71.7 ppm, with an average of 21.7 ppm) and Ta (0.52–31.6  
536 ppm, with an average of 9.20 ppm) contents. In comparison, those of HS-OB type  
537 crystallized from immiscible aqueous melt and HS-DG and HS-OG crystallized from  
538 exsolved fluid have significantly lower Nb and Ta contents (Figure 8j). The  
539 compositional variations of tourmaline are consistent with the petrographic  
540 observations, that is, columbite is commonly observed and paragenetic with  
541 disseminated tourmaline while absent in the tourmaline–quartz orbicules. It is thereby

542 inferred that Nb and Ta reached peak concentrations during the latest magmatic stage  
543 but were depleted in the exsolved aqueous B-rich melt/fluid in the Huotoushan case.  
544 Similar compositional variations were also reported in tourmaline from the Shangbao  
545 Nb-Ta granite, South China (Zhao et al., 2021b). Unfortunately, the REE contents in  
546 the different types of tourmaline from the two mineralized plutons exhibit low and  
547 variable contents (Figure 8k), providing limited information about their evolution and  
548 participation preference to melts or fluids. However, rare-earth minerals (e.g.,  
549 monazite, fluorocerite, and synchysite) are commonly observed in the granite matrix  
550 (Figure 3a–c) and the tourmaline-quartz veins (Figure 3d–f) but are rare in  
551 tourmaline-quartz orbicules, precluding the extraction effect of REE during the  
552 aqueous B-rich melt/fluid exsolution. The Sn content in tourmaline has been widely  
553 employed to predict Sn mineralization potential due to its high partition coefficient  
554 (Hong et al., 2017; Qiu et al., 2021). In our case, tourmaline from the orbicules  
555 (HS-OB and HS-OG) and rim of disseminated tourmaline (HS-DG) show  
556 significantly lower Sn contents compared to the HS-DB (Figure 8i), also arguing  
557 against the Sn enrichment in the B-rich melt and fluid phases during their exsolution.  
558 From this perspective, B-rich melt/fluid exsolution does not necessarily contribute to  
559 rare-metal mineralization.

560 As discussed above, the tourmaline-quartz orbicules resulted from exsolved  
561 B-rich melts in the late-stage crystallization of the Huoshibulake and Tamu granitic  
562 magmas, and the tourmaline-quartz veins represent another B-rich melt pulse from a  
563 deeper cogenetic magma chamber; both of them are regarded as the products of

564 magmatic-hydrothermal transition. However, a notable phenomenon is that the veins  
565 exhibit considerably higher Nb, Ta, Sn, and REE on both bulk rock and tourmaline  
566 scales (except for REE in tourmaline) with a higher abundance of rare-metal minerals  
567 compared to the orbicules. These rare-metal minerals show close paragenesis with  
568 fluorite; especially for acicular synchysite that only occurs as inclusions in fluorite  
569 (Figure 3d–f), linking fluorite saturation with REE and Nb precipitation. The  
570 relevance of fluorine and rare metals is also supported by the significantly higher  
571 whole-rock F, Nb, and  $\Sigma$ REE contents (1.10 wt%, 233 ppm, and 831 ppm,  
572 respectively, Wu et al., in preparation) of the tourmaline-quartz vein compared to  
573 those of the tourmaline-quartz orbicule (0.20 wt%, 84.9 ppm, and 208 ppm,  
574 respectively). These lines of evidence indicate that the timing when fluorite reaches  
575 saturation is a critical factor determining the concentration and precipitation of rare  
576 metals during the magmatic-hydrothermal process. Fluorine is considered an  
577 important agent for transporting Nb and REE as fluoride species (Williams-Jones et  
578 al., 2000; Ruberti et al., 2008). Thus, the saturation of fluorite can cause rapid  
579 depletion of the complexing ligand and simultaneously trigger the precipitation of  
580 these rare metals (Smith and Henderson, 2000). During the crystallization of the  
581 Huoshibulake and Tamu plutons, fluorite saturation occurred at the relatively early  
582 stage of the magmatic-hydrothermal transition and resulted in the disseminated  
583 crystallization of rare metals in the granite matrix; in contrast, fluorine in the parental  
584 magmas of the tourmaline-quartz veins was concentrated and fluorite did not reach  
585 saturation until their emplacement, leading to the veined rare-metal mineralization

586 after B-rich melts exsolution.

## 587 **IMPLICATIONS**

588 This study recognizes four generations of tourmaline formed from late magmatic,  
589 through magmatic-hydrothermal transition, to late hydrothermal stages in the  
590 Huoshibulake and Tamu alkali granites. The petrographic, compositional, and B  
591 isotopic variations recorded by the tourmaline provide valuable information for  
592 re-establishing the magmatic-hydrothermal processes. This study highlights the use of  
593 tourmaline as a tracer to unravel the magmatic-hydrothermal transition and related  
594 rare-metal mineralization in granitic systems. For instance, the differential rare-metal  
595 abundances between tourmalines from orbicules and veins are in good accordance  
596 with rare-metal mineral abundance. These observations, together with the close  
597 paragenesis of ore minerals and fluorite, further decode the critical role of fluorite  
598 saturation in rare-metal enrichment and mineralization during the transition. It is also  
599 important to note that when employing the compositional index of tourmaline (e.g.,  
600 Sn, which has been commonly used) to evaluate metallogenic potential, extra  
601 attention should be paid to the mineral structure and multi-generation crystallization.

## 602 **ACKNOWLEDGMENTS**

603 We thank Bei-Bei Pan and Hai-Zhou Li for their assistance during fieldwork. We  
604 extend our thanks to Yong-Jun Zhao, Kui-Dong Zhao, He-Dong Zhao, Di Zhang, and  
605 Chao Li for their help during the EPMA and LA-MC-ICP-MS analysis. We appreciate  
606 Andrea Dini and two anonymous reviewers for their insightful comments. We are  
607 grateful to chief editor Don Baker and associate editor Paul Tomascak for their

608 guidance and support throughout the review process.

609 **FUNDING**

610 This work was financially supported by National Natural Science Foundation of  
611 China (NSFC grant nos. 42173052 and 92162322) and the Shaanxi Provincial Natural  
612 Science Foundation Research Program (grant nos. 2023-JC-QN-0345 and  
613 2023-JC-YB-241). The visit of Huanhuan Wu at University of St Andrews was  
614 funded by the China Scholarship Council (No. 202206400021).

615

## REFERENCES CITED

- 616 Bai, T.B., Van Groos, A.F.K. (1999) The distribution of Na, K, Rb, Sr, Al, Ge, Cu, W,  
617 Mo, La, and Ce between granitic melts and coexisting aqueous fluids[J].  
618 *Geochimica et Cosmochimica Acta*, 63, 1117–1131.
- 619 Balen, D., and Broska, I. (2011) Tourmaline nodules: products of devolatilization  
620 within the final evolutionary stage of granitic melt? Geological Society, London,  
621 Special Publications, 350, 53–68.
- 622 Ballouard, C., Massuyeau, M., Elburg, M.A., Tappe, S., Viljoen, F., and Brandenburg,  
623 J.T. (2020) The magmatic and magmatic-hydrothermal evolution of felsic igneous  
624 rocks as seen through Nb-Ta geochemical fractionation, with implications for the  
625 origins of rare-metal mineralizations. *Earth-Science Reviews*, 203, 103115.
- 626 Ballouard, C., Poujol, M., Boulvais, P., Branquet, Y., Tartèse, R., and Vignerresse, J.L.  
627 (2016) Nb-Ta fractionation in peraluminous granites: A marker of the  
628 magmatic-hydrothermal transition. *Geology*, 44, 231–234.
- 629 Bassett, R.L. (1976) *The Geochemistry of Boron in Thermal Waters*, 307 p. Ph.D.  
630 thesis, Stanford University.
- 631 Borodulin, G.P., Chevychelov, V.Y., and Zaraysky, G.P. (2009) Experimental study of  
632 partitioning of tantalum, niobium, manganese, and fluorine between aqueous  
633 fluoride fluid and granitic and alkaline melts. *Doklady Earth Sciences*, 427, 868–  
634 873.
- 635 Carr, P., Norman, M.D., Bennett, V.C., and Blevin, P.L. (2021) Tin Enrichment in  
636 Magmatic-Hydrothermal Environments Associated with Cassiterite

- 637 Mineralization at Ardlethan, Eastern Australia: Insights from Rb-Sr and Sm-Nd  
638 Isotope Compositions in Tourmaline. *Economic Geology*, 116, 147–167.
- 639 Chen, F.W., Li, H.Q., and Lu, Y.F. (2002) Temporo-Spatial Distribution of Rare Metal  
640 and REE Deposits in Xinjiang, Northwest China. *Acta Geologica Sinica*, 76, 478–  
641 487.
- 642 Cheng, L., Zhang, C., Zhou, Y., Horn, I., Weyer, S. and Holtz, F., (2022) Experiments  
643 reveal enrichment of  $^{11}\text{B}$  in granitic melt resulting from tourmaline crystallisation.  
644 *Geochemical Perspectives Letters*, 20, 37–42.
- 645 Cheng, Z.G., Zhang, Z.C., Aibai, A., Kong, W.L., and Holtz, F. (2018) The role of  
646 magmatic and post-magmatic hydrothermal processes on rare-earth element  
647 mineralization: A study of the Bachu carbonatites from the Tarim Large Igneous  
648 Province, NW China. *Lithos*, 314–315, 71–87.
- 649 Chevychelov, V.Y., Zaraisky, G.P., Borisovskii, S.E., and Borkov, D.A. (2005) Effect of  
650 melt composition and temperature on the partitioning of Ta, Nb, Mn, and F  
651 between granitic (alkaline) melt and fluorine-bearing aqueous fluid: Fractionation  
652 of Ta and Nb and conditions of ore formation in rare-metal granites. *Petrology*, 13,  
653 305–321.
- 654 Dingwell, D.B., Pichavant, M., and Holtz, F. (1996) Chapter 8. Experimental studies of  
655 boron in granitic melts. In: Anovitz, L.M., Grew, E.S. (Eds.) *Boron*, 33, p. 331–  
656 386. *Reviews in Mineralogy and Geochemistry*, Mineralogical Society of America,  
657 Washington, D.C.
- 658 Drivenes, K., Larsen, R.B., Müller, A., Sørensen, B.E., Wiedenbeck, M., and Raanes,

- 659 M.P. (2015) Late-magmatic immiscibility during batholith formation: assessment  
660 of B isotopes and trace elements in tourmaline from the Land's End granite, SW  
661 England. *Contributions to Mineralogy and Petrology*, 169(6), 1–27.
- 662 Dutrow, B.L., and Henry, D.J. (2011) Tourmaline: A Geologic DVD. *Elements*, 7, 301–  
663 306.
- 664 Dyar, M.D., Wiedenbeck, M., Robertson, D., Cross, L.R., Delaney, J.S., Ferguson, K.,  
665 Francis, C.A., Grew, E.S., Guidotti, C.V., Hervig, R.L., and others (2001)  
666 Reference Minerals for the Microanalysis of Light Elements. *Geostandards and*  
667 *Geoanalytical Research*, 25, 441–463.
- 668 Gurenko, A.A., Veksler, I.V., Meixner, A., Thomas, R., Dorfman, A.M., and Dingwell,  
669 D.B. (2005) Matrix effect and partitioning of boron isotopes between immiscible  
670 Si-rich and B-rich liquids in the Si-Al-B-Ca-Na-O system: A SIMS study of  
671 glasses quenched from centrifuge experiments. *Chemical Geology*, 222, 268–280.
- 672 Halter, W.E., and Webster, J.D. (2004) The magmatic to hydrothermal transition and its  
673 bearing on ore-forming systems. *Chemical Geology*, 210(1–4), 1–6.
- 674 Harlaux, M., Kouzmanov, K., Gialli, S., Laurent, O., Rielli, A., Dini, A., Chauvet, A.,  
675 Menzies, A., Kalinaj, M., and Fontboté, L. (2020) Tourmaline as a Tracer of  
676 Late-Magmatic to Hydrothermal Fluid Evolution: The World-Class San Rafael  
677 Tin (-Copper) Deposit, Peru. *Economic Geology*, 115, 1665–1697.
- 678 Henry, D.J., and Dutrow, B.L. (1990) Ca substitution in Li-poor aluminous tourmaline.  
679 *The Canadian Mineralogist*, 28, 111–124.
- 680 Henry, D.J., and Dutrow, B.L. (2012) Tourmaline at diagenetic to low-grade

- 681 metamorphic conditions: Its petrologic applicability. *Lithos*, 154, 16–32.
- 682 Henry, D.J., and Guidotti, C.V. (1985) Tourmaline as a petrogenetic indicator mineral:  
683 an example from the staurolite-grade metapelites of NW Maine. *American*  
684 *Mineralogist*, 70, 1–15.
- 685 Henry, D.J., Novak, M., Hawthorne, F.C., Ertl, A., Dutrow, B.L., Uher, P., and Pezzotta,  
686 F. (2011) Nomenclature of the tourmaline-supergroup minerals. *American*  
687 *Mineralogist*, 96, 895–913.
- 688 Hervig, R.L., Moore, G.M., Williams, L.B., Peacock, S.M., Holloway, J.R., and  
689 Roggensack, K. (2002) Isotopic and elemental partitioning of boron between  
690 hydrous fluid and silicate melt. *American Mineralogist*, 87, 769–774.
- 691 Hong, W., Cooke, D.R., Zhang, L.J., Fox, N., and Thompson, J. (2017) Tourmaline-rich  
692 features in the Heemskirk and Pieman Heads granites from western Tasmania,  
693 Australia: Characteristics, origins, and implications for tin mineralization.  
694 *American Mineralogist*, 102, 876–899.
- 695 Hong, W., Fox, N., Cooke, D.R., Zhang, L.J., and Fayek, M. (2019) B- and O-isotopic  
696 compositions of tourmaline constrain late-stage magmatic volatile exsolution in  
697 Tasmanian tin-related granite systems. *Mineralium Deposita*, 55, 63–78.
- 698 Hou, K.J., Li, Y.H., Xiao, Y.K., Liu, F., and Tian, Y.R. (2010) In situ boron isotope  
699 measurements of natural geological materials by LA-MC-ICP-MS. *Chinese*  
700 *Science Bulletin*, 55, 3305–3311.
- 701 Huang, H., Wang, T., Zhang, Z.C., Li, C., and Qin, Q. (2018) Highly differentiated  
702 fluorine-rich, alkaline granitic magma linked to rare metal mineralization: A case

- 703 study from the Boziguo'er rare metal granitic pluton in South Tianshan Terrane,  
704 Xinjiang, NW China. *Ore Geology Reviews*, 96, 146–163.
- 705 Huang, H., Zhang, Z.C., Kusky, T., Santosh, M., Zhang, S., Zhang, D.Y., Liu, J.L., Zhao,  
706 Z.D. (2012) Continental vertical growth in the transitional zone between South  
707 Tianshan and Tarim, western Xinjiang, NW China: Insight from the Permian  
708 Halajun A1-type granitic magmatism. *Lithos*, 155, 49–66.
- 709 Huang, H., Zhang, Z.C., Santosh, M., Zhang, D.Y., and Wang, T. (2015) Petrogenesis of  
710 the Early Permian volcanic rocks in the Chinese South Tianshan: Implications for  
711 crustal growth in the Central Asian Orogenic Belt. *Lithos*, 228–229, 23–42.
- 712 Huang, R.F., and Audétat, A. (2012) The titanium-in-quartz (TitaniQ) thermobarometer:  
713 A critical examination and re-calibration. *Geochimica et Cosmochimica Acta*, 84,  
714 75–89.
- 715 Jiang, S.Y., Yu, J.M., and Lu, J.J. (2004) Trace and rare-earth element geochemistry in  
716 tourmaline and cassiterite from the Yunlong tin deposit, Yunnan, China:  
717 implication for migmatitic–hydrothermal fluid evolution and ore genesis.  
718 *Chemical Geology*, 209, 193–213.
- 719 Kaeter, D., Barros, R., Menuge, J.F., and Chew, D.M. (2018) The magmatic–  
720 hydrothermal transition in rare-element pegmatites from southeast Ireland:  
721 LA-ICP-MS chemical mapping of muscovite and columbite-tantalite. *Geochimica  
722 et Cosmochimica Acta*, 240, 98–130.
- 723 Kakihana, H., Kotaka, M., Satoh, S., Nomura, M., and Okamoto, M. (1977)  
724 Fundamental Studies on the Ion-Exchange Separation of Boron Isotopes. *Bulletin*

- 725 of the Chemical Society of Japan, 50, 158–163.
- 726 Kowalski, P. M., and Wunder, B. (2018) Boron isotope fractionation among vapor–  
727 liquids–solids–melts: experiments and atomistic modeling. In H. Marschall, and G.  
728 Foster, Eds, Boron isotopes: The Fifth Element, 7, p. 33–69. Advances in  
729 Geochemistry, Springer International Publishing, New York.
- 730 Linnen, R.L., Samson, I.M., Williams-Jones, A.E., and Chakhmouradian, A.R. (2014)  
731 Geochemistry of the Rare-Earth Element, Nb, Ta, Hf, and Zr Deposits. Treatise on  
732 Geochemistry, 13, 543–564.
- 733 Liu, T., and Jiang, S.Y. (2021) Multiple generations of tourmaline from Yushishanxi  
734 leucogranite in South Qilian of western China record a complex formation history  
735 from B-rich melt to hydrothermal fluid. American Mineralogist, 106, 994–1008.
- 736 Liu, Y.S., Hu, Z.C., Zong, K.Q., Gao, C.G., Gao, S., Xu, J., and Chen, H.H. (2010)  
737 Reappraisal and refinement of zircon U-Pb isotope and trace element analyses  
738 by LA-ICP-MS. Chinese Science Bulletin, 55, 1535–1546.
- 739 Long, Z.Y., Yu, X.Y., and Zheng, Y.Y. (2021) Ore formation of the Dayakou emerald  
740 deposit (Southwest China) constrained by chemical and boron isotopic  
741 composition of tourmaline. Ore Geology Reviews, 135, 104208.
- 742 Maner, J.L., and London, D. (2017) The boron isotopic evolution of the Little Three  
743 pegmatites, Ramona, CA. Chemical Geology, 460, 70–83.
- 744 Meyer, C., Wunder, B., Meixner, A., Romer, R.L., and Heinrich, W. (2008)  
745 Boron-isotope fractionation between tourmaline and fluid: an experimental  
746 re-investigation. Contributions to Mineralogy and Petrology, 156, 259–267.

- 747 Michaud, J.A.-S., and Pichavant, M. (2020) Magmatic fractionation and the  
748 magmatic-hydrothermal transition in rare metal granites: Evidence from  
749 Argemela (Central Portugal). *Geochimica et Cosmochimica Acta*, 289, 130–157.
- 750 Migdisov, A.A., and Williams-Jones, A.E. (2014) Hydrothermal transport and  
751 deposition of the rare earth elements by fluorine-bearing aqueous liquids.  
752 *Mineralium Deposita*, 49, 987–997.
- 753 Mohamed, M.A.M. (2013) Immiscibility between silicate magma and aqueous fluids in  
754 Egyptian rare-metal granites: melt and fluid inclusions study. *Arabian Journal of*  
755 *Geosciences*, 6, 4021–4033.
- 756 Nechaev, V.P., Dai, S., Zhao, L., Moore, T.A., and Nechaeva, E.V. (2021) The Tarim  
757 Basin, China, a prospect for plume-related Zr(Hf)-Nb(Ta)-REY-Ga-U  
758 mineralization. *Ore Geology Reviews*, 133, 104081.
- 759 Palmer, M.R., and Swihart, G.H. (1996) Chapter 13. Boron isotope geochemistry: an  
760 overview. In E.S. Grew, and L.M. Anovitz, Eds, *Boron*, 33, p. 709–744. *Reviews*  
761 *in Mineralogy*, Mineralogical Society of America, Washington, D.C.
- 762 Penniston-Dorland, S.C., Bebout, G.E., von Strandmann, P.A.E.P., Elliott, T., and  
763 Sorensen, S.S. (2012) Lithium and its isotopes as tracers of subduction zone fluids  
764 and metasomatic processes: Evidence from the Catalina Schist, California, USA.  
765 *Geochimica et Cosmochimica Acta*, 77, 530–545.
- 766 Qiu, K.F., Yu, H.C., Hetherington, C., Huang, Y.Q., Yang, T., and Deng, J. (2021)  
767 Tourmaline composition and boron isotope signature as a tracer of  
768 magmatic-hydrothermal processes. *American Mineralogist*, 106, 1033–1044.

- 769 Rozendaal, A., and Bruwer, L. (1995) Tourmaline nodules: indicators of hydrothermal  
770 alteration and Sn-Zn-(W) mineralization in the Cape Granite Suite, South Africa.  
771 *Journal of African Earth Sciences*, 21, 141–155.
- 772 Ruberti, E., Enrich, G.E., Gomes, C.B., and Comin-Chiaramonti, P. (2008)  
773 Hydrothermal REE fluorocarbonate mineralization at Barra do Itapirapua, a  
774 multiple stockwork carbonatite, Southern Brazil. *The Canadian Mineralogist*, 46,  
775 901–914.
- 776 Schmidt, B.C., Zotov, N., and Dupree, R. (2004) Structural implications of water and  
777 boron dissolution in albite glass. *Journal of non-crystalline solids*, 337, 207–219.
- 778 Schmidt, B.C., Thomas, R., and Heinrich, W. (2005) Boron speciation in aqueous fluids  
779 at 22 to 600°C and 0.1 MPa to 2 GPa. *Geochimica et Cosmochimica Acta*, 69,  
780 275–281.
- 781 Shuai, L., Liu, Z.Q., Tang, H., Yu, Z.C, Jia, T. (2019) Report of 1:50,000 mineral  
782 geological survey results in Huoshibulake area, Atushi City, Xinjiang (in Chinese),  
783 290 p. Non-ferrous minerals Geological survey Center, China.
- 784 Sheard, E.R., Williams-Jones, A.E., Heiligmann, M., Pederson, C., and Trueman, D.L.  
785 (2012) Controls on the Concentration of Zirconium, Niobium, and the Rare Earth  
786 Elements in the Thor Lake Rare Metal Deposit, Northwest Territories, Canada.  
787 *Economic Geology*, 107, 81–104.
- 788 Shi, P.C. (2010) Alkali-rich intrusive rocks and their metallogenic characteristics in  
789 Zambile area, Tianshan Mountain, southwest Xinjiang. *Xinjiang Nonferrous*  
790 *Metals*, 33, 1–5.

- 791 Slack, J.F. (1996) Chapter 11. Tourmaline associations with hydrothermal ore deposits.  
792 In E.S. Grew, and L.M. Anovitz, Eds, *Boron*, Boron, 33, p. 559–644. Reviews in  
793 Mineralogy, Mineralogical Society of America, Washington, D.C.
- 794 Slack, J.F., and Trumbull, R.B. (2011) Tourmaline as a Recorder of Ore-Forming  
795 Processes. *Elements*, 7, 321–326.
- 796 Smith, M.P., and Yardley, B.W.D. (1996) The boron isotopic composition of tourmaline  
797 as a guide to fluid processes in the southwestern England orefield: An ion  
798 microprobe study. *Geochimica et Cosmochimica Acta*, 60, 1415–1426.
- 799 Smith, M.P., and Henderson, P. (2000) Preliminary fluid inclusion constraints on fluid  
800 evolution in the Bayan Obo Fe-REE-Nb deposit, Inner Mongolia, China.  
801 *Economic Geology*, 95, 1371–1388.
- 802 Sokół, K., Finch, A.A., Hutchison, W., Cloutier, J., Borst, A.M., and Humphreys,  
803 M.C.S. (2021) Quantifying metasomatic high-field-strength and rare-earth  
804 element transport from alkaline magmas. *Geology*, 50, 305–310.
- 805 Thomas, R., Davidson, P., and Beurlen, H. (2012) The competing models for the origin  
806 and internal evolution of granitic pegmatites in the light of melt and fluid inclusion  
807 research. *Mineralogy and Petrology*, 106, 55–73.
- 808 Thomas, R., and Davidson, P. (2016) Revisiting complete miscibility between silicate  
809 melts and hydrous fluids, and the extreme enrichment of some elements in the  
810 supercritical state—Consequences for the formation of pegmatites and ore  
811 deposits. *Ore Geology Reviews*, 72, 1088–1101.
- 812 Thomas, R., Förster, H.J., and Heinrich, W. (2003) The behaviour of boron in a

- 813 peraluminous granite-pegmatite system and associated hydrothermal solutions: a  
814 melt and fluid-inclusion study. *Contributions to Mineralogy and Petrology*, 144,  
815 457–472.
- 816 Thomas, R., Forster, H.J., Rickers, K., and Webster, J.D. (2005) Formation of  
817 extremely F-rich hydrous melt fractions and hydrothermal fluids during  
818 differentiation of highly evolved tin-granite magmas: a melts/fluids-inclusion  
819 study. *Contributions to Mineralogy and Petrology*, 148, 582–601.
- 820 Timofeev, A., Migdisov, A.A., and Williams-Jones, A.E. (2015) An experimental study  
821 of the solubility and speciation of niobium in fluoride-bearing aqueous solutions at  
822 elevated temperature. *Geochimica et Cosmochimica Acta*, 158, 103–111.
- 823 Tonarini, S., Pennisi, M., Adorni-Braccesi, A., Dini, A., Ferrara, G., Gonfiantini, R.,  
824 Wiedenbeck, M., and Gröning, M. (2003a) Intercomparison of Boron Isotope and  
825 Concentration Measurements. Part I: Selection, Preparation and Homogeneity  
826 Tests of the Intercomparison Materials. *Geostandards and Geoanalytical Research*,  
827 27, 21–39.
- 828 Tonarini, S., Forte, C., Petrini, R., and Ferrara, G. (2003b) Melt/biotite  $^{11}\text{B}/^{10}\text{B}$  isotopic  
829 fractionation and the boron local environment in the structure of volcanic glasses.  
830 *Geochimica et Cosmochimica Acta*, 67, 1863–1873.
- 831 Trumbull, R.B., and Chaussidon, M. (1999) Chemical and boron isotopic composition  
832 of magmatic and hydrothermal tourmalines from the Sinceni granite–pegmatite  
833 system in Swaziland. *Chemical Geology*, 153, 125–137.
- 834 Trumbull, R.B., Codeço, M.S., Jiang, S.Y., Palmer, M.R., and Slack, J.F. (2020) Boron

- 835 isotope variations in tourmaline from hydrothermal ore deposits: A review of  
836 controlling factors and insights for mineralizing systems. *Ore Geology Reviews*,  
837 125, 103682.
- 838 Trumbull, R.B., Krienitz, M.S., Gottesmann, B., and Wiedenbeck, M. (2007) Chemical  
839 and boron-isotope variations in tourmalines from an S-type granite and its source  
840 rocks: the Erongo granite and tourmalinites in the Damara Belt, Namibia.  
841 *Contributions to Mineralogy and Petrology*, 155, 1–18.
- 842 Trumbull, R.B., and Slack, J.F. (2018) Boron Isotopes in the Continental Crust:  
843 Granites, Pegmatites, Felsic Volcanic Rocks, and Related Ore Deposits. In H.  
844 Marschall, and G. Foster, Eds, *Boron Isotopes: The Fifth Element*, 7, p. 249–272.  
845 *Advances in Geochemistry*, Springer International Publishing, New York.
- 846 Vasyukova, O., and Williams-Jones, A. E. (2014) Fluoride–silicate melt immiscibility  
847 and its role in REE ore formation: Evidence from the Strange Lake rare metal  
848 deposit, Québec-Labrador, Canada. *Geochimica et Cosmochimica Acta*, 139,  
849 110–130.
- 850 Van Hinsberg, V.J., Henry, D.J., and Dutrow, B.L. (2011) Tourmaline as a Petrologic  
851 Forensic Mineral: A Unique Recorder of Its Geologic Past. *Elements*, 7, 327–332.
- 852 Veksler, I.V., Thomas, R., and Schmidt, C. (2002) Experimental evidence of three  
853 coexisting immiscible fluids in synthetic granitic pegmatite. *American*  
854 *Mineralogist*, 87, 775–779.
- 855 Wei, X., Xu, Y.G., He, B., Zhang, L., Xia, X.P., and Shi, X.F. (2019) Zircon U-Pb age  
856 and Hf-O isotope insights into genesis of Permian Tarim felsic rocks, NW China:

- 857 Implications for crustal melting in response to a mantle plume. *Gondwana*  
858 *Research*, 76, 290–302.
- 859 Williams-Jones, A.E., Samson, I.M., and Olivo, G.R. (2000) The genesis of  
860 hydrothermal fluorite-REE deposits in the Gallinas Mountains, New Mexico.  
861 *Economic Geology*, 95, 327–341.
- 862 Williams-Jones, A.E., and Vasyukova, O.V. (2023) Niobium, Critical Metal, and  
863 Progeny of the Mantle. *Economic Geology*, 118, 837–855.
- 864 Xie, M.C., Xiao, W.J., Su, B.X., Sakyi, P.A., Ao, S.J., Zhang, J.E., Song, D.F., Zhang,  
865 Z.Y., Li, Z.Y., and Han, C.M. (2021) REE mineralization related to carbonatites  
866 and alkaline magmatism in the northern Tarim basin, NW China: implications for  
867 a possible Permian large igneous province. *International Journal of Earth Sciences*,  
868 111, 2759–2776.
- 869 Yang, S.Y., Jiang, S.Y., Zhao, K.D., Dai, B.Z., and Yang, T. (2015) Tourmaline as a  
870 recorder of magmatic–hydrothermal evolution: an in situ major and trace element  
871 analysis of tourmaline from the Qitianling batholith, South China. *Contributions*  
872 *to Mineralogy and Petrology*, 170(5–6), 1–21.
- 873 Yang, W.B., Niu, H.C., Li, N.B., Hollings, P., Zurevinski, S., and Xing, C.M. (2020)  
874 Enrichment of REE and HFSE during the magmatic-hydrothermal evolution of the  
875 Baerzhe alkaline granite, NE China: Implications for rare metal mineralization.  
876 *Lithos*, 358–359, 105411.
- 877 Zaraisky, G.P., Aksyuk, A.M., Devyatova, V.N., Udoratina, O.V. and Chevychelov, V.Y.  
878 (2009) The Zr/Hf ratio as a fractionation indicator of rare-metal granites.

- 879 Petrology, 17, 25–45.
- 880 Zraisky, G.P., Korzhinskaya, V., and Kotova, N. (2010) Experimental studies of Ta<sup>2</sup>O<sup>5</sup>  
881 and columbite–tantallite solubility in fluoride solutions from 300 to 550°C and 50  
882 to 100 MPa. Mineralogy and Petrology, 99, 287–300.
- 883 Zhang, C.L., Xu, Y.G., Li, Z.X., Wang, H.Y., and Ye, H.M. (2010) Diverse Permian  
884 magmatism in the Tarim Block, NW China Genetically linked to the Permian  
885 Tarim mantle plume. Lithos, 119, 537–552.
- 886 Zhang, C.L., and Zou, H.B. (2013) Permian A-type granites in Tarim and western part  
887 of Central Asian Orogenic Belt (CAOB): Genetically related to a common  
888 Permian mantle plume? Lithos, 172–173, 47–60.
- 889 Zhang, R.X., and Yang, S.Y. (2016) A Mathematical Model for Determining Carbon  
890 Coating Thickness and Its Application in Electron Probe Microanalysis. Microsc  
891 Microanal, 22, 1374–1380.
- 892 Zhao, H.D., Zhao, K.D., Palmer, M.R., and Jiang, S.Y. (2019) In-situ elemental and  
893 boron isotopic variations of tourmaline from the Sanfang granite, South China:  
894 Insights into magmatic-hydrothermal evolution. Chemical Geology, 504, 190–  
895 204.
- 896 Zhao, H.D., Zhao, K.D., Palmer, M.R., Jiang, S.Y., and Chen, W. (2021a)  
897 Magmatic-Hydrothermal Mineralization Processes at the Yidong Tin Deposit,  
898 South China: Insights from In Situ Chemical and Boron Isotope Changes of  
899 Tourmaline. Economic Geology, 116, 1625–1647.
- 900 Zhao, Z., Yang, X.Y., Liu, Q.Y., Lu, Y.Y., Chen, S.S., Sun, C., Zhang, Z.Z., Wang, H.,

- 901 and Li, S. (2021b) In-situ boron isotopic and geochemical compositions of  
902 tourmaline from the Shangbao Nb–Ta bearing monzogranite, Nanling Range:  
903 Implication for magmatic-hydrothermal evolution of Nb and Ta. *Lithos*, 386–387,  
904 106010.
- 905 Zhao, Z., Yang, X.Y., Lu, Y.Y., Zhang, Z.Z., Chen, S.S., Sun, C., Hou, Q., Wang, Y., and  
906 Li, S. (2022) Geochemistry and boron isotope compositions of tourmalines from  
907 the granite-greisen-quartz vein system in Dayishan pluton, Southern China:  
908 Implications for potential mineralization. *American Mineralogist*, 107, 495–508.
- 909 Zheng, B.Q., Chen, B., Sun, K.K., and Huang, C. (2022) Tourmaline as a recorder of  
910 the magmatic-hydrothermal evolution in the formation of pegmatite: In-situ  
911 elemental and boron isotopic compositions of tourmaline from the Qinghe  
912 pegmatite, Chinese Altay orogen. *Journal of Asian Earth Sciences*, 231, 105224.
- 913 Zhu, Z.Y., Wang, R.C., Che, X.D., Zhu, J.C., Wei, X.L., and Huang, X.E. (2015)  
914 Magmatic–hydrothermal rare-element mineralization in the Songshugang granite  
915 (northeastern Jiangxi, China): Insights from an electron-microprobe study of Nb–  
916 Ta–Zr minerals. *Ore Geology Reviews*, 65, 749–760.
- 917 Zong, Z.J., Du, Y.S., Li, S.T., Cao, Y., Du, J.G., Deng, X.H., and Xue, L.W. (2020)  
918 Petrogenesis of the early Permian A-type granites in the Halajun region, southwest  
919 Tianshan, western Xinjiang, NW China: implications for geodynamics of Tarim  
920 large igneous province. *International Geology Review*, 63, 1110–1131.
- 921

922

## FIGURE CAPTIONS

923 Figure 1 **(a)** Geological map of the South Tianshan Belt and the northern margin of the  
924 Tarim Craton, modified from [Gao et al. \(2011\)](#) and [Huang et al. \(2015\)](#). **(b)** Simplified  
925 geological map of the Huoshibulake pluton. **(c)** Simplified geological map of the Tamu  
926 pluton.

927

928 Figure 2 **(a–c)** Field photo showing the contact relationship between the Huoshibulake  
929 pluton and the surrounding rock. **(b and c)** Photographs of hand specimens of  
930 disseminated tourmaline, showing dispersed tourmaline crystals in the Huoshibulake  
931 K-feldspar biotite granite and biotite granite, respectively. **(d and e)** Plane polarized  
932 light photomicrographs of sub- to euhedral tourmaline, with brown-yellow pleochroism  
933 at the core and blue-green pleochroism at the rim. **(f)** Plane polarized light  
934 photomicrograph of anhedral tourmaline aggregate. **(g–i)** BSE images of disseminated  
935 tourmaline. Orange circles and blue circles with numbers show the analyzed location  
936 and  $\delta^{11}\text{B}$  values for boron isotopic analysis, respectively. Tur = tourmaline, Qz = quartz,  
937 Kfs = K-feldspar, Pl = plagioclase, Bt = biotite, Flr = fluorite, Mnz = monazite, Zrn =  
938 zircon, Clb = columbite.

939

940 Figure 3 BSE images of disseminated tourmaline from the Huoshibulake pluton **(a–c)**  
941 and vein tourmaline from the Huoshibulake **(d)** and the Tamu **(e and f)** plutons showing  
942 the close paragenesis between fluorite and rare-metal minerals. **(a)** Typical  
943 disseminated tourmaline with abundant inclusions of columbite, fluorite, and monazite;

944 **(b)** a strongly mineralized area with abundant fluocerite and synchysite showing  
945 paragenesis with fluorite; **(c)** anhedral columbite and abundant acicular synchysite  
946 included in a fluorite grain; **(d)** a large amount of rare-earth minerals (synchysite,  
947 fluocerite, and monazite) and columbite deposited in a F-rich domain; **(e and f)**  
948 columbite and acicular synchysite crystallized in fluorite droplets. Tur = tourmaline, Qz  
949 = quartz, Kfs = K-feldspar, Ms = muscovite, Flr = fluorite, Mnz = monazite, Clb =  
950 columbite, Fert = fluocerite, Zrn = zircon, Syn = synchysite.

951

952 Figure 4 **(a and b)** Photographs of outcrops of tourmaline-quartz orbicules from the  
953 Huoshibulake and Tamu plutons, showing typical core-mantle-rim texture. **(c and d)**  
954 Plane polarized light photomicrograph of sieve-like tourmaline intergrown with quartz,  
955 showing the yellow-brown core and blue-green rim. **(e and f)** BSE images of orbicular  
956 tourmaline with dark cores and light rims. Orange circles and blue circles with numbers  
957 show the analyzed location and  $\delta^{11}\text{B}$  values for boron isotope, respectively. Tur =  
958 tourmaline, Qz = quartz, Flr = fluorite, Mnz = monazite.

959

960 Figure 5 Photographs showing texture, mineralogy, and B isotopic characteristics of  
961 tourmaline-quartz veins in the Huoshibulake and Tamu plutons. **(a and b)**  
962 Near-parallel tourmaline-quartz veins outcrops; **(c)** hand specimen photo showing the  
963 sub- to euhedral tourmaline intergrowth with quartz and fluorite; **(d–f)** plane polarized  
964 light photomicrograph of tourmaline grains with growth zonation and near identical B  
965 isotopic compositions. Tourmaline grains **(d)** are sectioned oblique to the c axis, and **(e**

966 **and f)** parallel to the c axis. Orange circles and blue circles with numbers show the  
967 analyzed location and  $\delta^{11}\text{B}$  values for boron isotope, respectively. **(g–i)** Representative  
968 BSE images showing the concentric zoning in tourmaline hosted in the veins. Tur =  
969 tourmaline, Qz = quartz, Flr = fluorite.

970

971 Figure 6 **(a)** Classification diagrams based on X-site occupancy (modified after [Henry](#)  
972 [et al. 2011](#)) and **(b)** Al-Fe-Mg ternary diagrams (modified after [Henry and Guidotti,](#)  
973 [1985](#)) of tourmaline from the Huoshibulake and Tamu plutons showing compositional  
974 variations of tourmaline from various source rocks. 1 = Li-rich granitoid pegmatites  
975 and aplites, 2 = Li-poor granitoids and their associated pegmatites and aplites, 3 =  
976  $\text{Fe}^{3+}$ -rich quartz-tourmaline rocks (hydrothermally altered granites), 4 = metapelites  
977 and metapsammities coexisting with an Al-saturating phase, 5 = metapelites and  
978 metapsammities not coexisting with an Al-saturating phase, 6 =  $\text{Fe}^{3+}$ -rich  
979 quartz-tourmaline rocks, calc-silicate rocks, and metapelites, 7 = low-Ca  
980 metaultramafics and Cr, V-rich sediments, 8 = metacarbonates and metapyroxenites.  
981 M1 =  $\text{Fe}^{3+}\text{Al}_1$  and  $(\text{Fe}^{2+}, \text{OH}^-)(\text{Al}, \text{O}^{2-})_{-1}$ , M2 =  $(\text{Mg}, \text{OH}^-)(\text{Al}, \text{O}^{2-})_{-1}$ . HS =  
982 Huoshibulake pluton, TM = Tamu pluton, DB = yellow-brown core of disseminated  
983 tourmaline, DG = blue-green rim of disseminated tourmaline, OB = yellow-brown core  
984 of orbicular tourmaline, OG = blue-green rim of orbicular tourmaline, V = vein  
985 tourmaline.

986

987 Figure 7 **(a and b)** Classification of tourmaline from the Huoshibulake and Tamu

988 plutons (modified after [Trumbull and Chaussidon, 1999](#); [Henry and Dutrow, 2012](#)); (**c–**  
989 **f**) Chemical discrimination diagrams for tourmaline from the Huoshibulake and Tamu  
990 plutons, showing their compositional evolution trends and exchange vectors (modified  
991 after [Henry and Dutrow 1990, 2012](#)). Abbreviations are same as Figure 6.

992

993 Figure 8 Box plots showing comparisons of selected major element (apfu, **a–d**) and  
994 trace element (ppm, **e–k**) compositions in different tourmaline types from the  
995 Huoshibulake and Tamu plutons. The “N” values in the table are numbers of analyzed  
996 spots. Abbreviations are same as Figure 6.

997

998 Figure 9 Trace element variation diagrams of tourmaline from the Huoshibulake and  
999 Tamu plutons, showing the positive correlations between different element pairs.  
1000 Abbreviations are same as Figure 6.

1001

1002 Figure 10 Box plots showing variations of boron isotopic compositions in different  
1003 types of tourmaline. Abbreviations are same as Figure 6.

1004

1005 Figure 11 Modeling of B isotopic fractionation between (**a**) melt and tourmaline and  
1006 (**b**) fluid and tourmaline. The initial  $\delta^{11}\text{B}$  values of the melt and aqueous fluid are set  
1007 as -12.3‰ and -8.3‰, respectively. See text for details. The violin plots show the  
1008 ranges of B isotopic compositions of different tourmaline types. Abbreviations are  
1009 same as Figure 6.

1010

1011 Figure 12 Idealized scenarios showing the formation of the different types of  
1012 tourmaline. Generation I: during the late-stage crystallization of the plutons, B  
1013 reached saturation and crystallized as disseminated tourmaline. Generation II: with  
1014 continuous crystallization, the immiscibility of B-rich aqueous melts resulted in the  
1015 crystallization of orbicular tourmaline. Generation III: exsolved fluids formed the  
1016 overgrowths of tourmaline at the rims of the earlier magmatic tourmaline. Generation  
1017 IV: another pulse of B-rich aqueous melts intruded into fractures of the consolidated  
1018 granite. Abbreviations are same as Figure 6.

1019

Figure 1

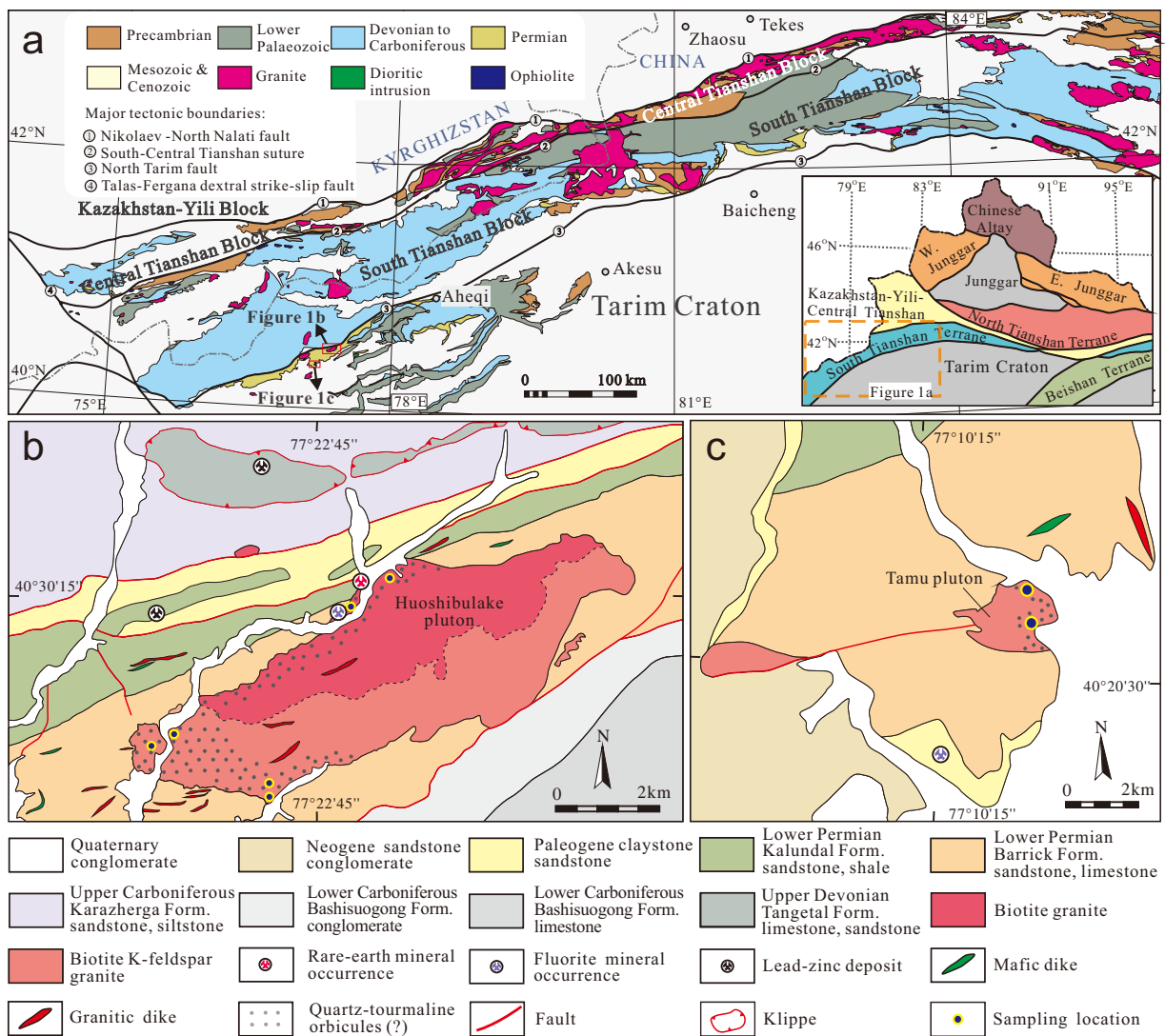


Figure 2

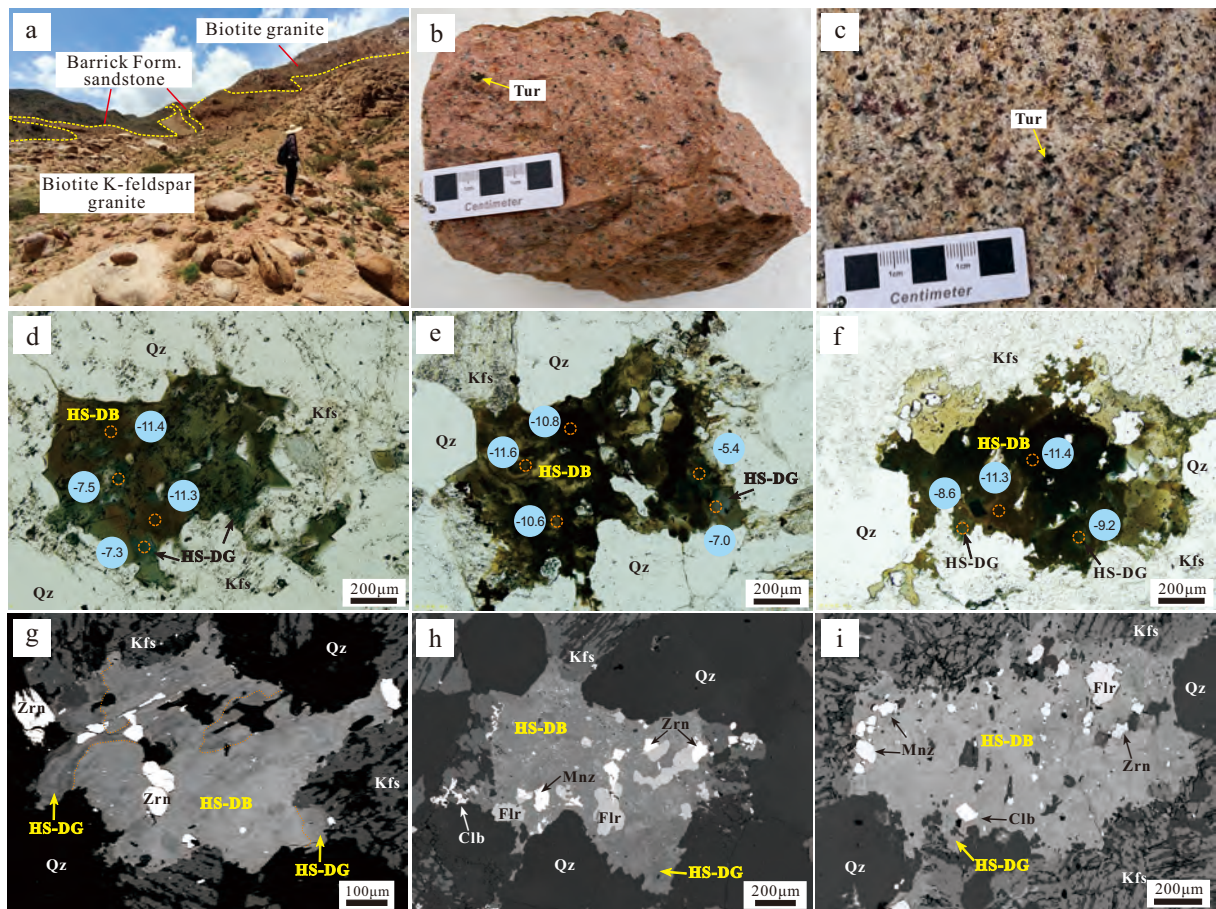


Figure 3

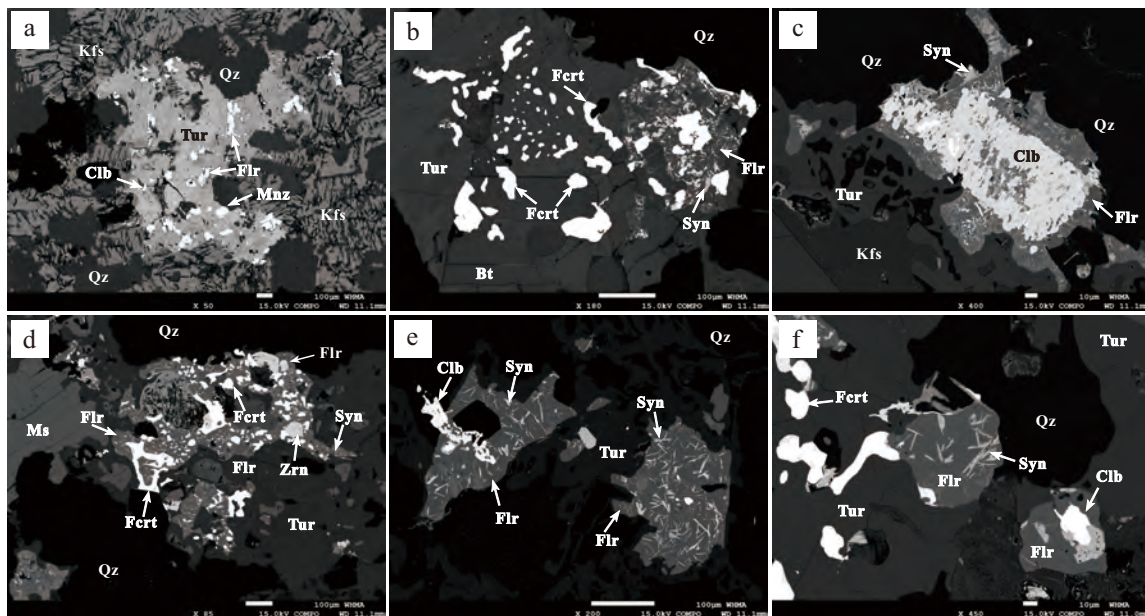


Figure 4

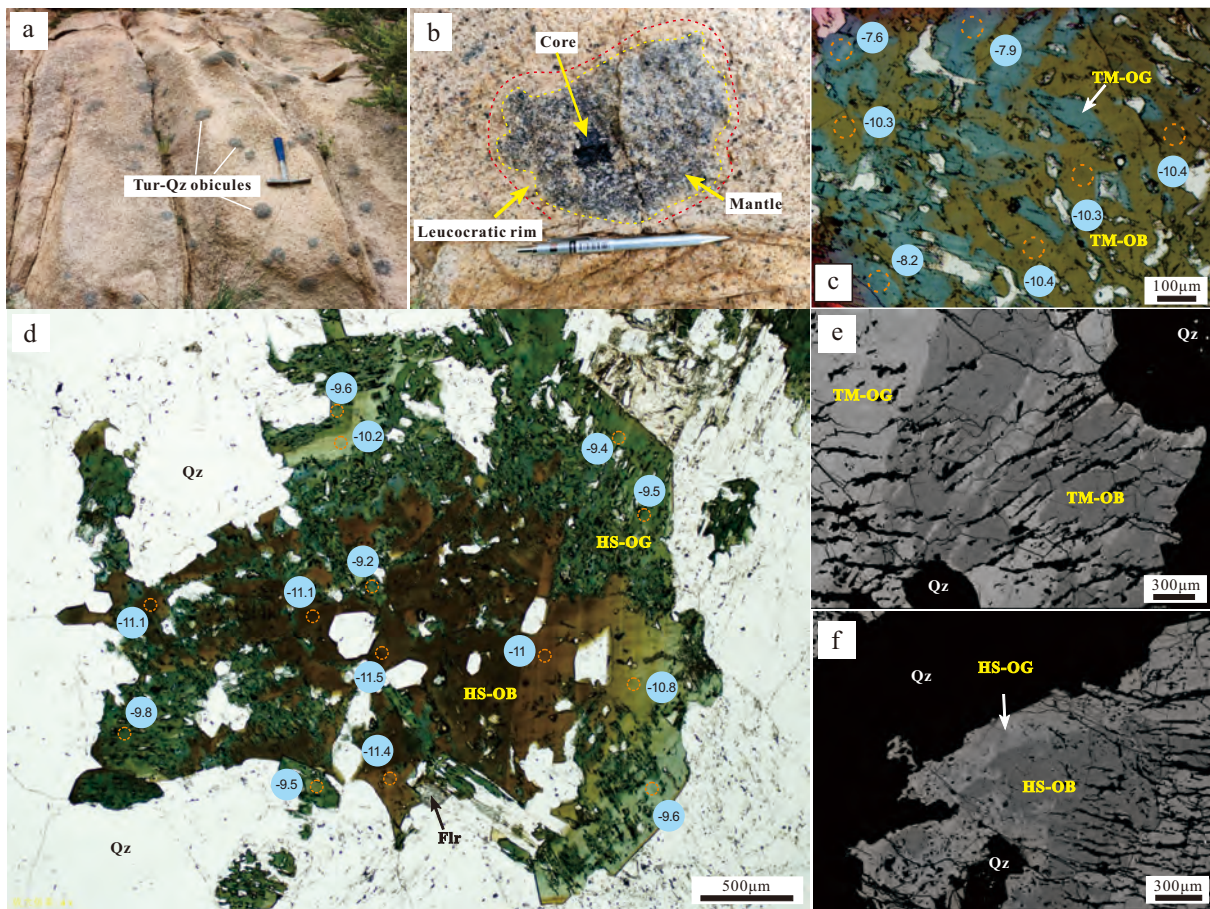


Figure 5

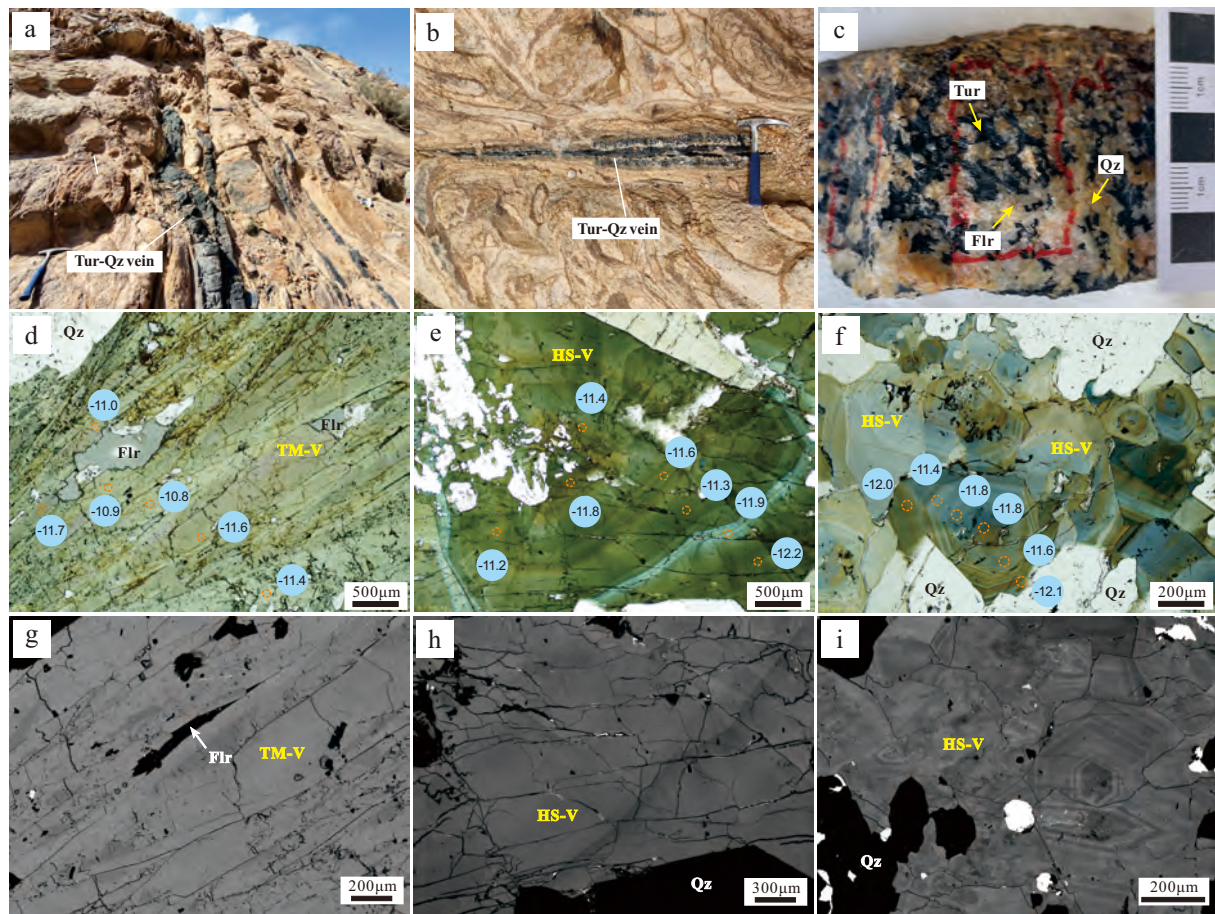


Figure 6

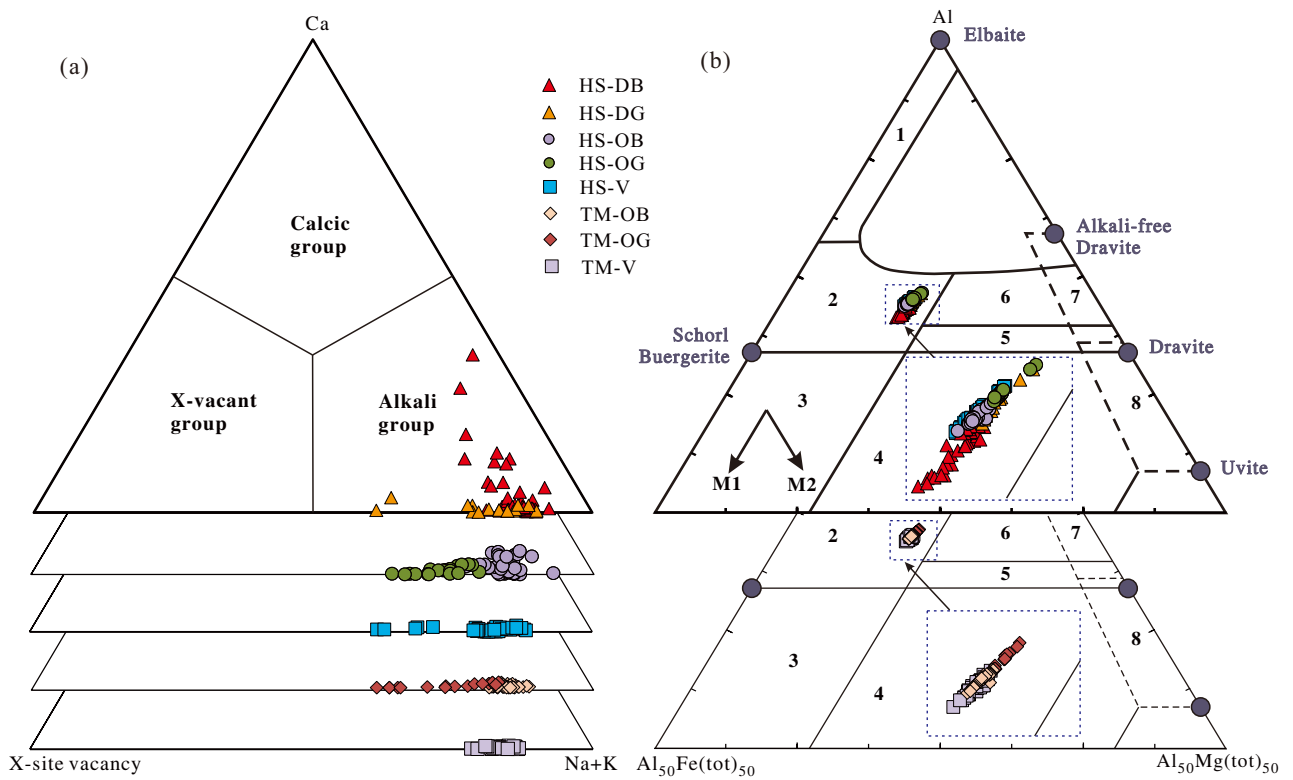


Figure 7

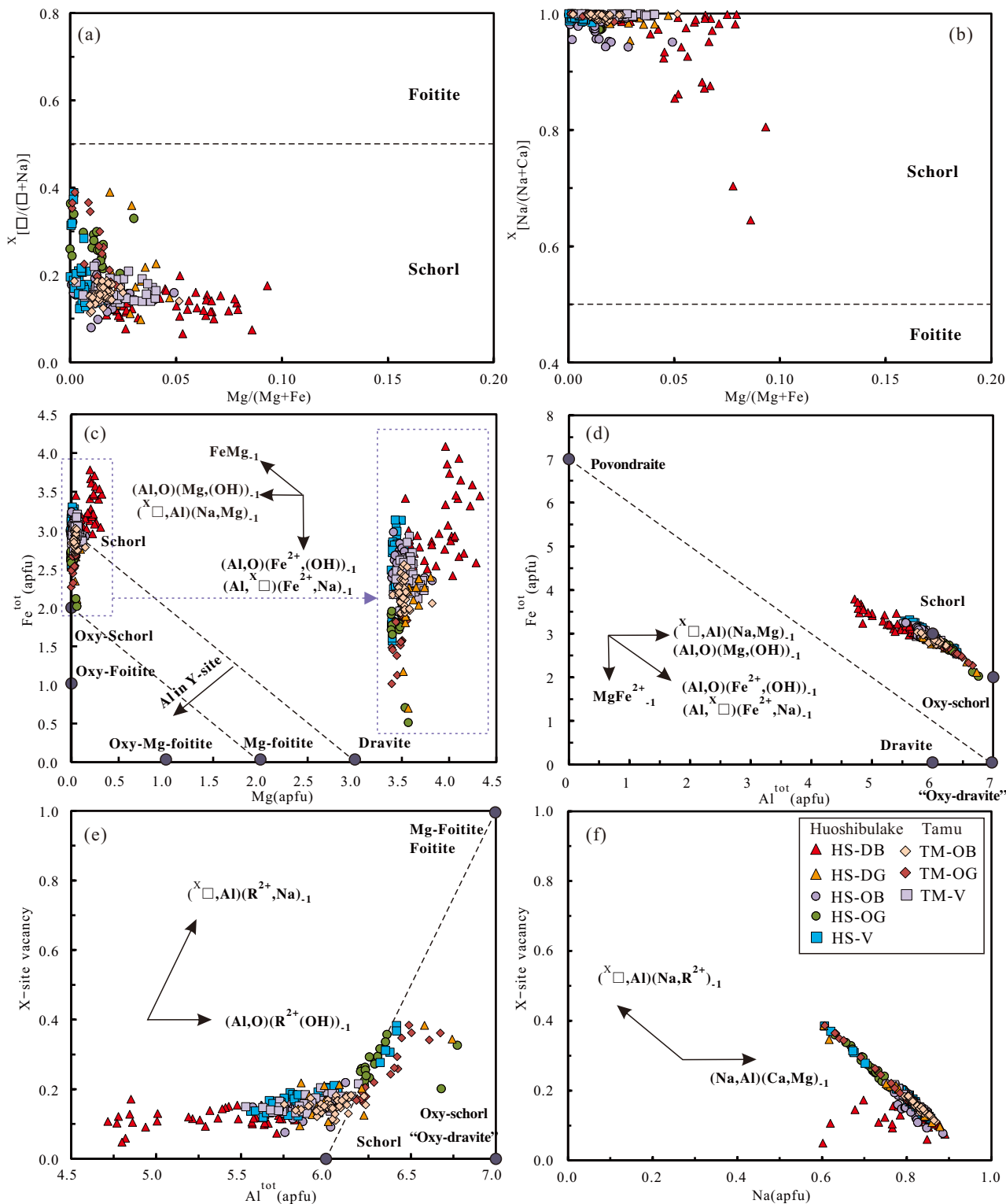


Figure 8

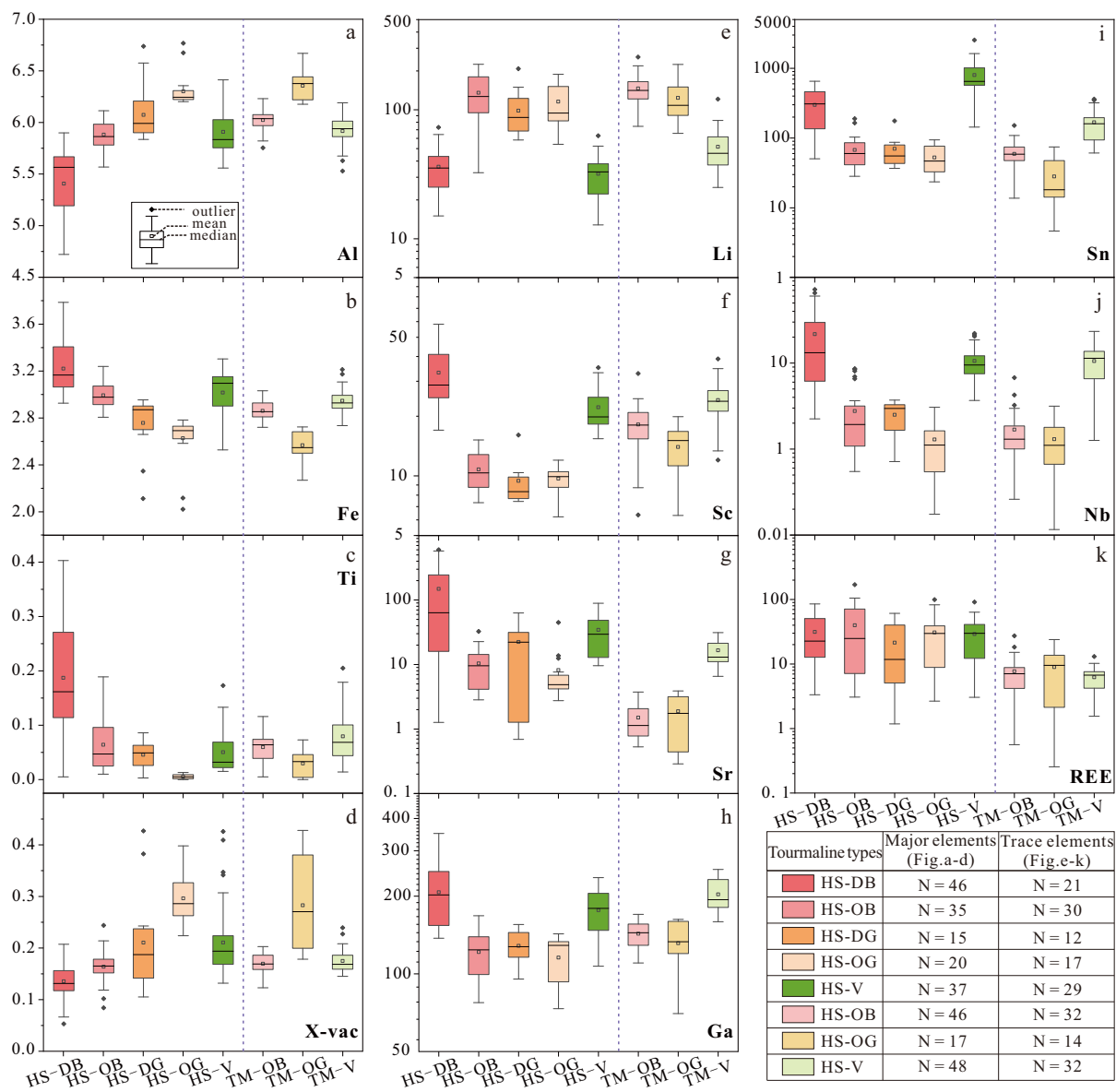


Figure 9

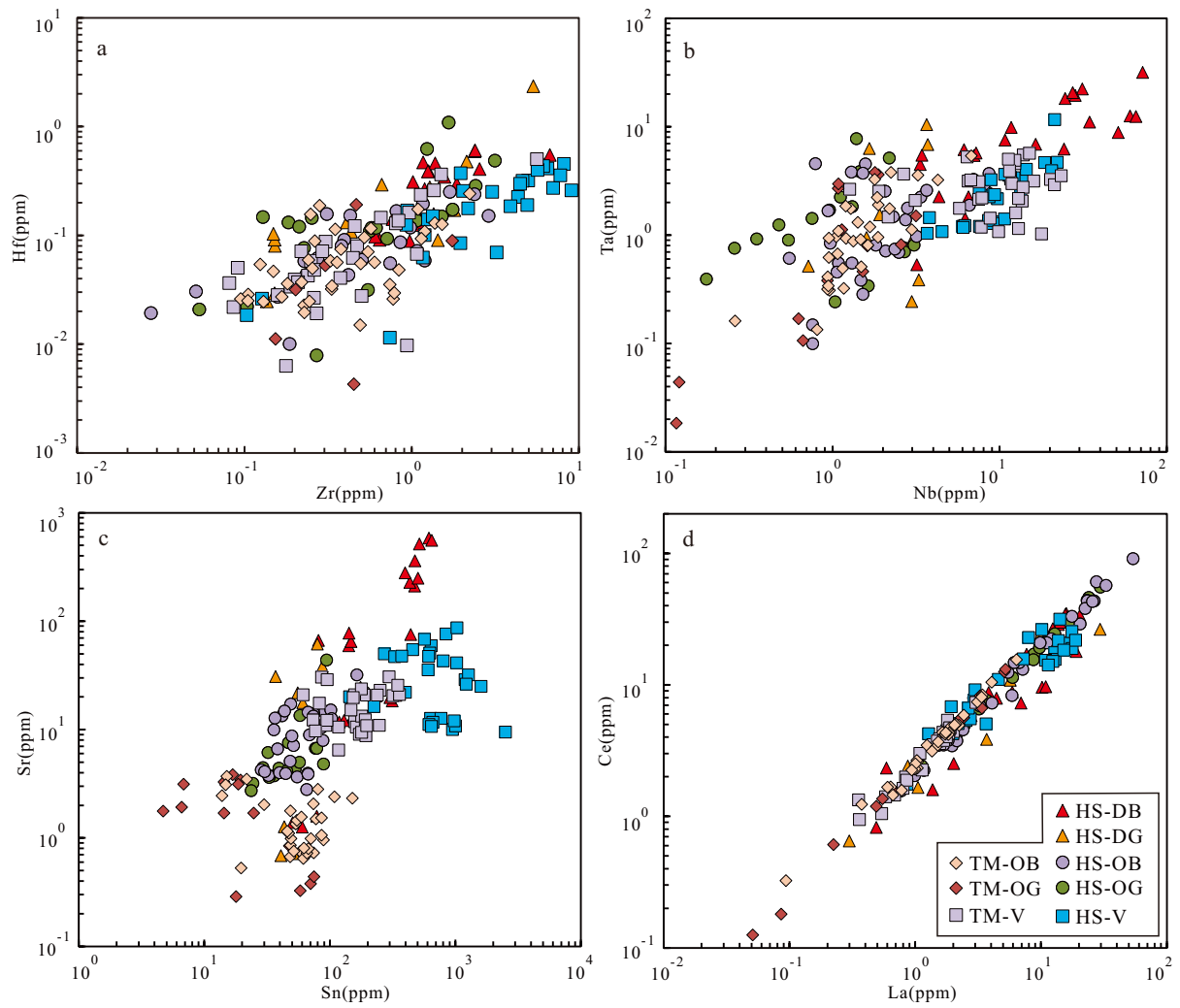


Figure 10

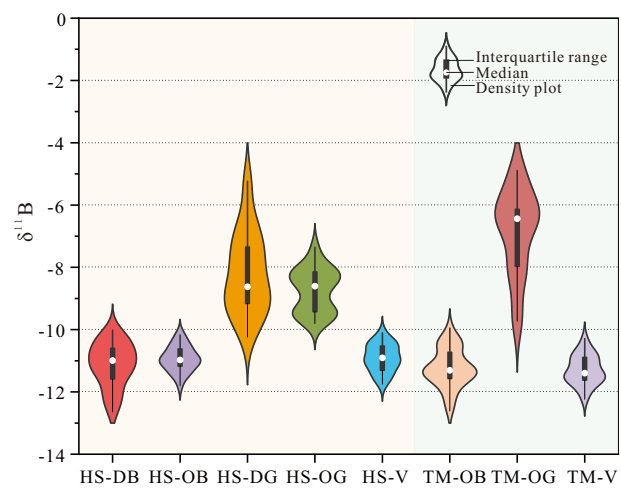


Figure 11

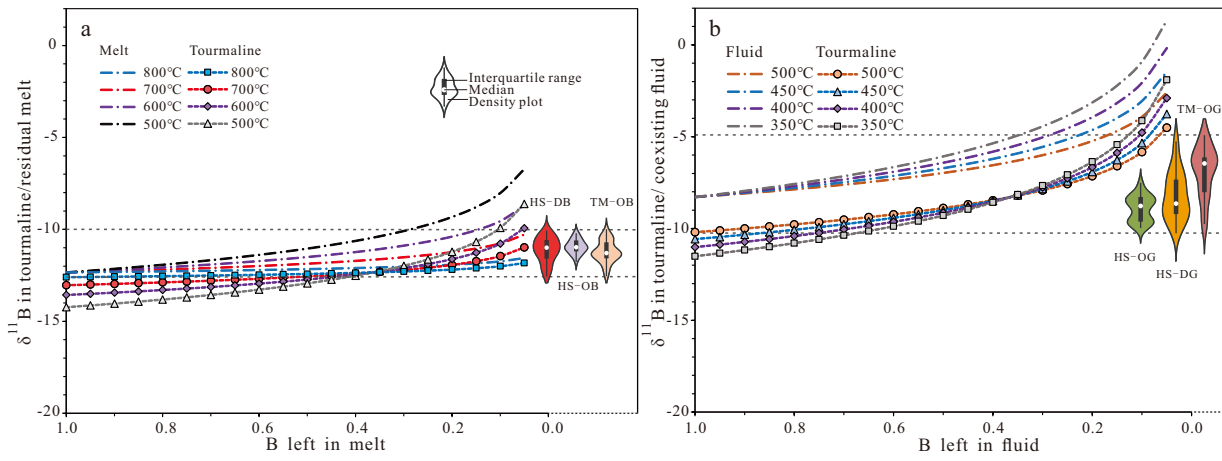


Figure 12

